Ni-Cu-Co-rich hydrothermal manganese mineralization in the Wallis and Futuna back-arc environment (SW Pacific)

Ewan Pelleter [a,*], Yves Fouquet [a], Joël Etoubleau [a], Sandrine Cheron [a], Shasa Labanieh [a], Pierre Josso [a], Claire Bollinger [c], Jessica Langlade [b]

[a] Ifremer – Unité de Recherche Géosciences Marines, F-29280 Plouzané, France
[b] CNRS, Ifremer c/Brest, F-29280 Plouzane, France
[c] Institut Universitaire Européen de la Mer, UMS 3113, Plouzané, France

ARTICLE INFO

ABSTRACT

The Wallis and Futuna back-arc system is a complex area composed of at least two active oceanic spreading centers (the Futuna and Alofi spreading centers) and young volcanic zones characterized by diffuse magmatism locally affected by the Samoan hotspot. This geological setting is favorable to the establishment of hydrothermal systems, in the form of either high-temperature (HT) hydrothermal venting or low-temperature (LT) diffuse flow. During the 2010 Futuna cruise aboard the R/V L'Atalante, three remarkable inactive LT Fe-Si-Mn deposits were discovered (Utu Uli, Anakele and Utu Sega). Some of the Mn-rich precipitates discovered exhibit the highest base metals concentrations so far recorded in ferromanganese rocks, including in the well-documented hydrogenetic crusts and polymetallic nodules. The deposits lie on top of volcanoes and formed in close association with the volcanic facies. The manganese mineralization occurs in the form of massive layered crusts and Mn-rich cements within strongly altered basaltic pyroclastic rocks, brecciated lavas and, more rarely, in sediments. Field observations and mineralogical and chemical studies support a hydrothermal origin for the mineralization and show that nickel, cobalt and copper enrichments are controlled by the precipitation of 7 Å and 10 Å manganates. The conventional geochemical classifications (e.g. Bonatti et al., 1972) used to decipher the origin of Mn mineralization cannot be used for this new type of deposit and new robust discrimination diagrams need to be established. We suggest that the unusual enrichment of metals recorded in our samples is due to (i) a lack of precipitation of high-temperature massive sulfides at depths that would have retained metals (e.g. Cu, Ni, Co); (ii) isolation of the hydrothermal system, thereby avoiding Ni, Co and Cu losses in the water column; and (iii) the ability of birnessite and buserite/todorokite to scavenge Co, Ni, and Cu from aqueous fluids. The Utu Uli and Anakele deposits share certain characteristics with the active hydrothermal system at Loihi seamount (e.g. the depth of mineralization, relationships with pyroclastic volcanoes, and the influence of a mantle plume source) and thus might represent late-stage products of this specific type of hydrothermal activity. Elsewhere, the Co-rich mineralization of the Calatrava volcanic field (CVF) in Spain may be a potential analog of the Utu Sega deposit. The Mn-(Co) deposits of the CVF formed in close proximity to Pliocene volcanic rocks. Metals were transported by epithermal hydrothermal solutions with high fO_2 and cobalt was scavenged by Mn oxides. Together with the well-documented stratabound Mn deposits (González et al., 2016; Hein et al., 2008; Hein et al., 1996), the Mn deposits discovered in the Wallis and Futuna back-arc provide crucial insights into LT hydrothermal activity in the deep ocean. The metal-rich character of this LT hydrothermal activity may be of major importance for future research on the net flux of hydrothermally derived metals (e.g. Ni, Co, Cu) to the open ocean.

© 2016 Elsevier B.V. All rights reserved.

1. Introduction

Ferromanganese mineralization occurs in nearly all deep-sea environments and is produced by three main processes (Hein et al., 1997): (i) precipitation of iron and manganese oxyhydroxides colloids from cold ambient seawater, (ii) precipitation from pore waters and (iii) precipitation from hydrothermal fluids. The first two of these processes lead to the formation of ferromanganese crusts and polymetallic nodules, respectively, whereas the third mechanism is related to the formation of Fe-Mn $\pm$ Si deposits. With a narrow range of Fe/Mn ratios (Fe/Mn = ~1) and high concentrations of Co, Ni, Cu, REE (Rare Earth Elements), HFSE (High Field Strength Elements), and Te and Pt, ferromanganese crusts are regarded as a potential mineral resource (Hein

* Corresponding author.
E-mail address: ewan.pelleter@ifremer.fr (E. Pelleter).

et al., 2013). Polymetallic nodules exhibit a wide range of Fe/Mn ratios (1 to 15) and metals contents (Cronan, 1997; Dymond et al., 1984) and may be of economic interest for Cu and Ni in specific environments (e.g. in the Clarion-Clipperton fracture zone). Ferromanganese deposits that precipitated from hydrothermal processes show a broad range of compositions, ranging from pure Mn oxides to almost pure Fe oxides with the highly variable amount of amorphous silica and/or nontronite. They usually exhibit low to very low metals contents as a result of sulfide fractionation at depth (e.g. Glasby et al., 1997; Hein et al., 2008), minor metals leaching of igneous rocks by low temperature (LT) hydrothermal fluids and/or discharge of metals to the water column prior to Mn oxyhydroxides precipitation. However, several stratabound hydrothermal Mn deposits in back-arc basins (e.g. Fouquet et al., 1993; Kuhn et al., 2003), active hot spot volcanoes (Hein et al., 1996; Hein et al., 1992), arc system (Hein et al., 2008; Hein et al., 1990) and margin setting (González et al., 2016) have been shown to display slightly anomalous trace element contents (e.g. Mo, Ni, Cd, Zn, Cd, Cu, Co). These deposits are generally interpreted to be the distal precipitates of high-temperature (HT) systems that produce massive sulfides and sulfates (Hein et al., 2008; Kuhn et al., 2003).

In 2010, exploration of the French exclusive economic zone (EEZ) of Wallis and Futuna during the Futuna cruise led to the discovery of three remarkable hydrothermal ferromanganese deposits (Utu Uli, Anakele and Utu Sega; Fig. 1). This paper describes the sampled Fe-Si-Mn precipitates, some of which exhibit the highest base metals concentrations so far recorded in ferromanganese rocks, including in the well-documented hydrogenetic crusts and polymetallic nodules (Hein et al., 2015; Hein

et al., 1997). The objective of this study is to document these atypical Fe-Si-Mn precipitates, which provide crucial insights into LT hydrothermal activity in the deep ocean.

2. Geological setting and sampling sites

The Wallis, Futuna and Alofi islands are located along a key part of the Pacific-Australia plate boundary. The area is bordered by the North Fiji fracture zone, the active Tonga-Kermadec subduction zone and associated Lau and North Fiji back-arc basins and, the currently active Samoan plume. The tectonic/geological setting, between the northern end of the Tonga trench and the regional Fiji transform fault, accounts for the complex volcanic and tectonic activity in the area. Previous investigations have revealed multiple active extensional zones including well-organized spreading centers such as the FUTUNA and ALOFI oceanic ridge (Fouquet et al., 2015; Pelletier et al., 2001)(Fig. 1) and several areas of numerous and diffuse magmatic centers (e.g. the Southeast Futuna volcanic zone; Pelletier et al., 2001). Located west of Futuna Island, the 20–30° trending Futuna spreading center is composed of a series of en echelon spreading segments. From an interpretation of magnetic anomalies, the opening rate of the oceanic ridge is estimated to be 4 cm/yr (Pelletier et al., 2001). South-east of Futuna Island, bathymetric maps and reflectivity data clearly reveals that active extension and recent volcanism occur throughout the Southeast Futuna volcanic zone and along the Alofi spreading center (Fouquet et al., 2015; Pelletier et al., 2001).

The geochemical compositions of the lavas collected during the FUTUNA cruise are related to partial melting of an Indian-like mantle that
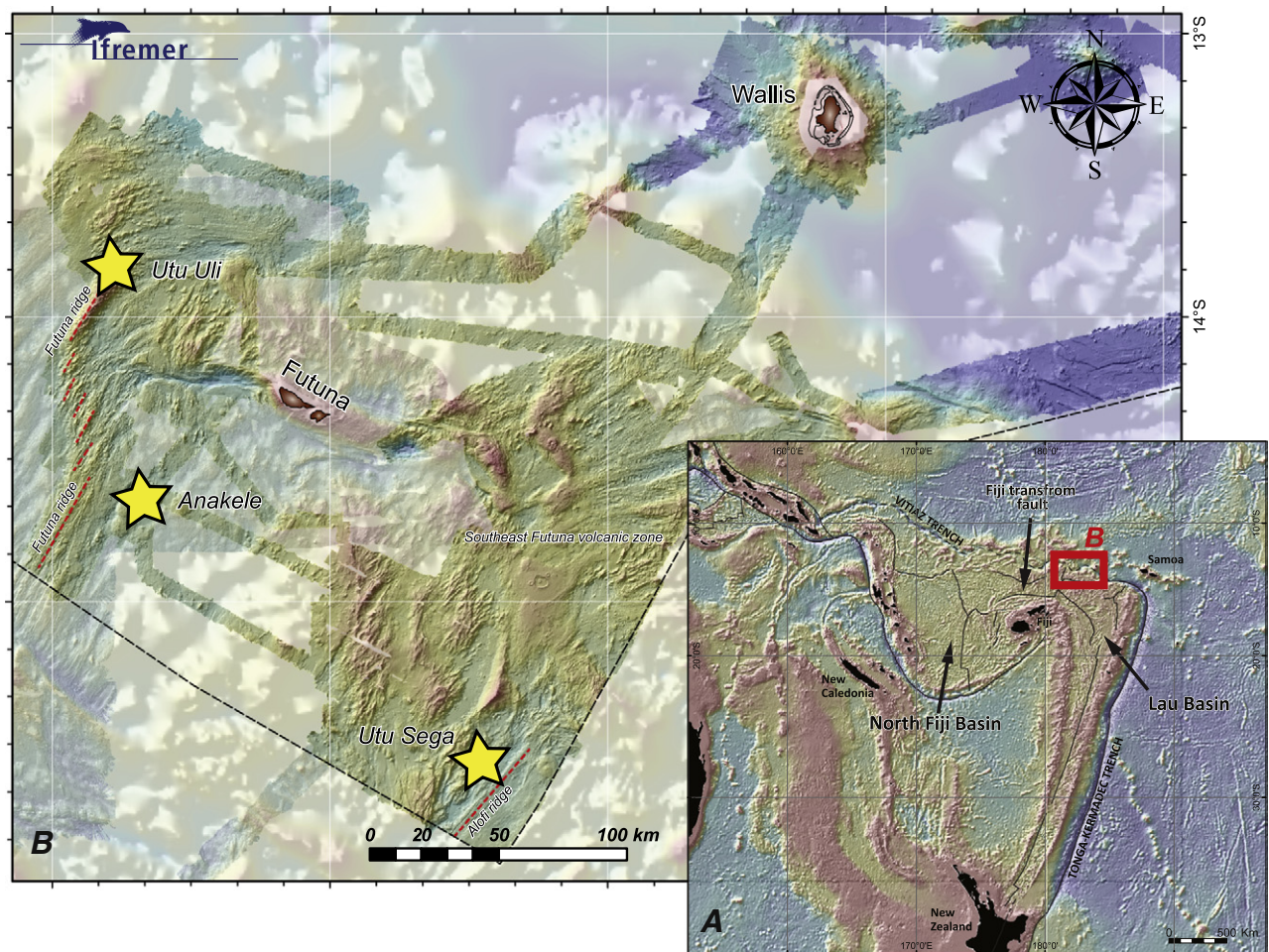

Fig. 1. A. Main geodynamic features of the South-West Pacific region and location of the study area (B); B. Locations of the Utu Uli, Anakele and Utu Sega ferromanganese deposits (Wallis and Futuna region, SW-Pacific).

has been significantly metasomatized by an enriched end-member composed of Samoan plume material (Labanieh et al., 2011). The influence of the Samoan plume is strongest to the west of Futuna Island, and particularly in the northern part of the Futuna spreading center.
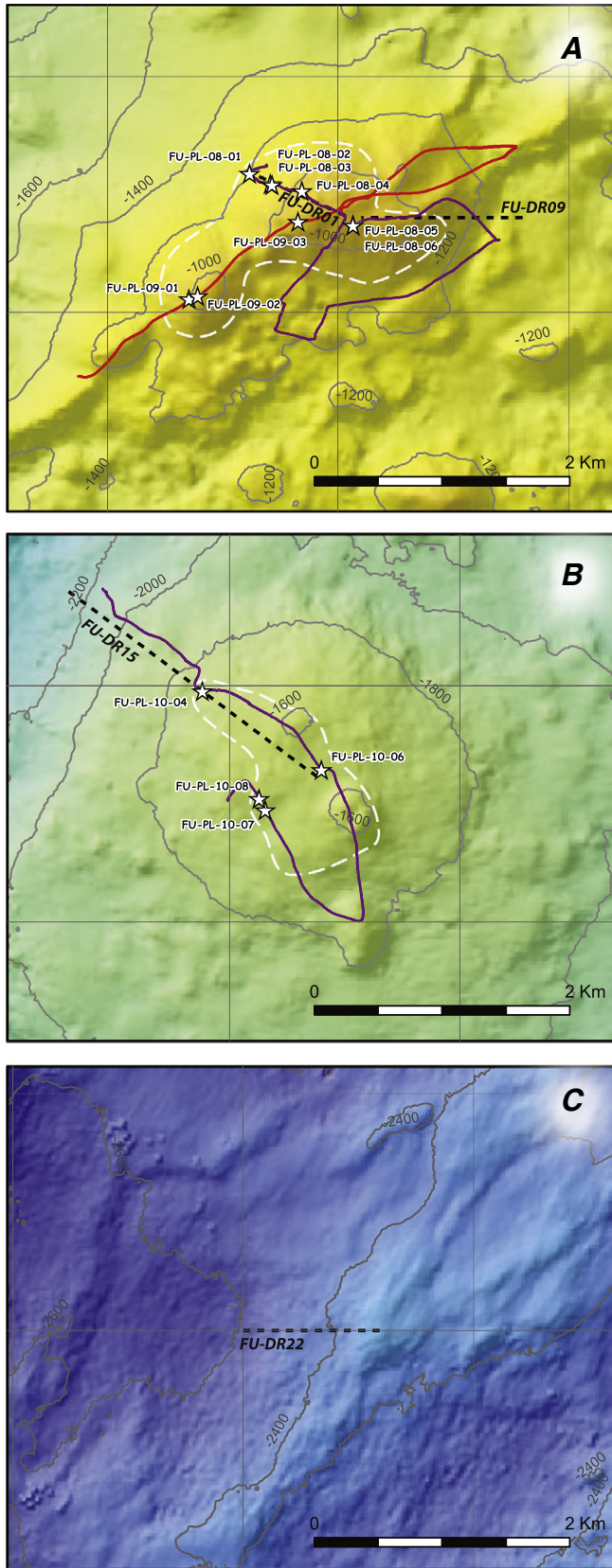
The Utu Uli deposit is located at the northern tip of the Futuna oceanic ridge axis. Two manned submersible dives and two dredge operations were successfully carried out during the 2010 FUTUNA cruise. The deposit is controlled by a line of small sub-circular volcanoes (Fig. 2A). These edifices are mainly composed of pyroclastic rocks and highly vesicular basaltic pillows lavas that exhibit a trace elements chemical composition similar to that of the Oceanic Island Basalt (OIB) of the Samoan plume (Labanieh et al., 2011). The manganese mineralization (Fig. 3A, B, and C) is found 800 m to 1000 m below sea level (mbsl) and covers at least three distinct volcanic edifices over a total surface area of approximately 1.5 km^2 (~1.5 km × 1 km). On the flank of the volcanoes, the manganese mineralization consists of layered Mn crusts up to 5 cm in thickness. The bathymetric highs exhibit both layered crust with bread-crust-like fractures (Fig. 3A) and decimetric-to-metric-sized mounds. Locally, the manganese crust is crosscut by iron and silica-rich crest and/or veins, up to 1 m in height, which likely reflect pulses of hydrothermal activity (Fig. 3 B, C).

The Anakele deposit is located on a broad (~5 km × 5 km) pancake-like volcano, 20 km east of the southern part of the Futuna ridge. Observations were carried out during a manned submersible dive and additional sampling was performed during a dredge operation (Fig. 2B). The manganese mineralization (Fig. 3D, E, and F) was observed at the top of the volcanic edifice. The magmatic rocks are composed of pyroclastic rocks and basaltic pillows lavas that are in places covered by a thick sedimentary cover and, in rare instances, by a 1-cm-thick hydrogenetic Fe-Mn crust. The two topographic highs close to the top (>1600 mbsl) of the edifice may represent small individual pyroclastic volcanoes. These are systematically covered by manganese mineralization. Due to significant sediment accumulations in the depressions, the continuity of the mineralization is unclear. However, the mineralized area, present between 1750 to 1560 mbsl might be as extensive as the Utu'Uli mineralization (~1.5 km^2). The manganese oxyhydroxides form smooth to granular layered Mn crusts that are crosscut by Fe-Si-rich precipitates. The yellow, reddish yellow and red colour of the material immediately below the crusts (Fig. 3D, E) is related to the high proportion of iron oxyhydroxides and a minor amount of yellow nontronite.

The Utu Sega deposit was sampled by dredging on a NNE-SSW trending ridge located 5 km west of the Alofi oceanic ridge axis (Fig. 1 and Fig. 2). The volcanic rocks collected include strongly altered basaltic pillow lavas and volcanic breccias. The mineralization is dominated by dense and laminated manganese precipitates.

While a hydrothermal character of the mineralization is expected from in-situ observations, no evidence for active hydrothermal discharge has yet been found in the close vicinity of the three deposits.

3. Samples and methods

Samples were collected during the FUTUNA cruise aboard the R/V L'Atalante in 2010. This cruise was dedicated to regional mapping and exploration for polymetallic sulfides in the French Exclusive Economic Zone (EEZ) around the Wallis and Futuna Islands. A series of dredge hauls and dives (HOV Nautile) were undertaken in order to sample the mineralization. Selected samples were labeled according to the name of the cruise (FU for FUTUNA), the type of sampling (DR for dredge hauls; PL for diving operations), the number of the operation and a rock designation number (e.g. FU-DR15-01). Samples were characterized and prepared directly on-board. Rocks were cut and dried in

Fig. 2. Bathymetric maps of the three Mn deposits (locations in Fig. 1). A. Bathymetric map of Utu Uli deposit; the purple line and red line correspond to the tracks of dive FU-PL08 and dive FU-PL09, respectively. B. Bathymetric map of Anakele deposit; the purple line represents the tracks of dive FU-PL10. C. Bathymetric map of Utu Sega deposit. The black dotted lines mark the tracks of the dredge hauls; the white stars mark the locations of samples collected during dive operations; and the white dotted lines show the spatial extent of the Mn mineralization.
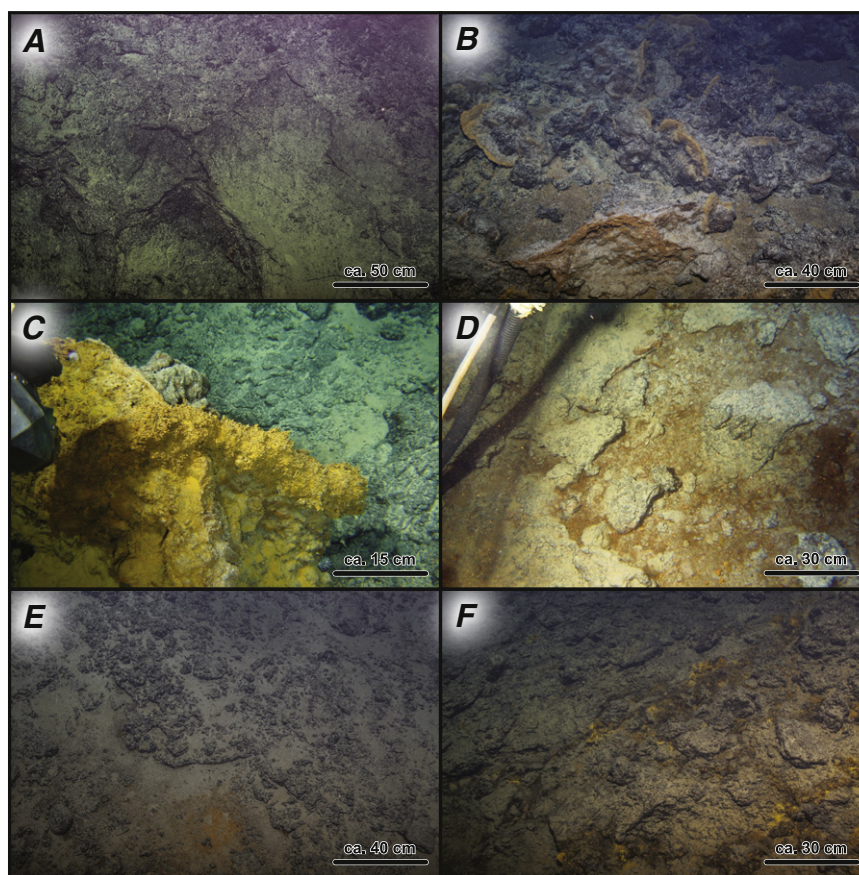
Fig. 3. Frame captures from FU-PL08, FU-PL09 and FU-PL10 HOV Nautile Dive video. A. Layered and massive Mn oxide crust; the surface often exhibits bread-crust-like fracturing (Utu Uli). B. Mn mineralization crosscut by Fe-Si-rich crests composed of amorphous iron oxyhydroxides and opal (Utu Uli). C. Large Fe-Si-rich crest with worm tubes on the top (Utu Uli). D. Iron oxides-rich layer outcropping beneath a 3 to 5-cm-thick Mn crust (Anakele). E. Mn crust with a granular texture overlying iron oxides and nontronite (Anakele). F. Fe-Si-rich mineralization that has precipitated through fractures within a thick (≥10 cm) Mn crust (Anakele).

an air oven at 50 °C. A representative portion of each sample was ground to a fine powder using an agate mortar.

Mineralogical and quantitative chemical data were acquired using X-ray techniques (X-ray diffraction and X-ray fluorescence) at the Laboratoire de Géochimie et Métallogénie at IFREMER institute (Brest, France).

X-ray diffraction (XRD) analyses were conducted with a BRUKER AXS D8 Advance and a BRUKER D2 PHASER diffractometer. Samples were top loaded into 2.5 cm diameter circular cavity holders, and all analyses were run between 5° and 70°2θ, in steps of 0.01°2θ at 1 s/step (monochromatic Cu Kα radiation, 40 kV, 30 mA). Minerals were identified using Diffrac.Suite EVA software. This method allowed most of the minerals in the samples to be identified (e.g. silicates, carbonates, well-crystallized manganates, well-crystallized oxyhydroxides). For manganates characterization, analyses were performed directly on board and two month later in the laboratory. Additionally, selected samples were re-analyzed five years later in order to evaluate the possible collapse of 10 Å magnanates to 7 Å manganates over time.

For characterization of the clays, a separated fraction (<2 μm) was investigated on two types of oriented mounts (air-dried and glycol-saturated) from 2 to 40°2θ, in steps of 0.01°2θ, at 1 s/step (monochromatic Cu Kα radiation, 40 kV, 30 mA). A randomly oriented sample was prepared in order to identify trio- or dioctahedral clay minerals (e.g. nontronite) from the 060 reflections (57 to 64° 2θ, in steps of 0.02°2θ, at 120 s/step).

X-ray fluorescence analyses were conducted with a wavelength dispersive X-ray fluorescence spectrometer (WD-XRF; BRUKER AXS S8 TIGER) on fusion beads (for major elements) or compressed pellets (for trace elements). After data acquisition, the measured net peak intensities corrected for inter-element effects were converted into concentrations using calibration curves generated from analysis of certified geochemical standard powders (measured under identical analytical conditions). Rare earth elements were analyzed by inductively coupled plasma mass spectrometry (ELEMENT2 HR-ICP-MS) at the Pôle Spectrométrie Océan (Brest, France) (see Josso et al., this volume for analytical procedures).

Scanning electron microscopy (SEM) investigations were performed with a FEI Quanta 200 SEM on C-coated polished sections and on small fragments (1 mm × 1 mm) of manganese mineralization. Secondary electron and backscattered images were acquired for textural characterization of the Mn oxides.

Mineral analyses were performed on C-coated polished sections using a Cameca SX100 electron microprobe (Microsonde Ouest, Brest, France) operated in wavelength dispersive mode. Operating conditions for spot analyses were set to 15 keV, 20 nA and a 10 s counting time on the peak (spot size = 1 μm). The φ(ρZ) matrix correction of Pouchou and Pichoir (1988) was applied. The standards (element, emission line) used were albite (Na kα, Si Kα), InP (P kα), forsterite (Mg kα), corundum (Al kα), orthose (K kα), wollastonite (Ca kα), synthetic manganese titanate (Mn kα, Ti kα), pure iron (Fe kα), pure cobalt (Co kα), pure nickel (Ni kα), pure copper (Cu kα), sphalerite (Zn kα), pure molybdenum (Mo kα), barytine (Ba kα). X-ray quantitative element maps were generated using SX100 software. The analytical setup used for point analyses was also used for the mapping, and a common set of calibration intensities was therefore used for quantification of both point and map data. Electron microprobe spot analyses and

chemical maps were performed to evaluate both the differences among Mn oxides precipitated in contact with seawater (i.e. layered massive microcrystalline crust) or developed at the subsurface and the differences between the crystallites (C), microcrystallites (MC) and amorphous cryptocrystalline (AC) Mn oxides.

A Pearson coefficient correlation matrix was calculated for the i) whole data set ($n = 35$), ii) volcanic- and/or sediment-free mineralized samples ($n = 21$), iii) Utu Uli volcanic- and/or sediment-free mineralized samples ($n = 14$) and iv) Anakele mineralized samples ($n = 10$) (Supplementary Tables S1, S2, S3 and S4). Si, Al, Fe, Mn, Ca, Mg, K, Na, Ti, P, V, Co, Ni, Cu, Zn, As, Sr, Y, Ba, Mo were taken into account in order to extract information on possible phase and/or element associations. The zero correlations were calculated at the 95% confidence interval and statistically significant correlations were highlighted.

4. Results

4.1. Sample morphology and mineralogy

We studied a total of 35 mineralized samples (Utu Uli: $n = 20$; Anakele: $n = 10$; Utu Sega: $n = 5$) encompassing a wide range of mineralogical and geochemical types, from pure Mn oxide to nearly pure Fe-Si rocks with variable amounts of altered pyroclastic rocks and minor sediments.

At Utu'Uli and Anakele, the mineralization developed directly on the seafloor and consists of a black manganese crust (up to 2-cm-thick) composed of dense and massive Mn oxyhydroxides with a metallic gray luster (Fig. 4A) and Fe-Si crests composed of X-ray amorphous iron oxyhydroxides and opal (Fig. 4B). The mineralization directly beneath the layered crust displays a breccia-like texture resulting from Mn oxyhydroxides cementation of highly vesicular lapilli, volcanic bombs and glass shards (Fig. 4C, D). The pyroclastic material is strongly altered and the pristine mineralogy has typically been completely replaced by nontronite and/or iron and manganese oxyhydroxides (Fig. 4C). One sample (FU-DR-01-03; Fig. 4A) provides an outstanding section of the first centimeter of the mineralization, showing the 2-cm-thick massive and laminated crust overlying the fully altered, Mn-cemented pyroclastic rocks. Several samples display striking mineralogical zoning composed, from top to bottom, of Mn oxides, Fe oxides and yellow to green nontronite (Fig. 4D). The thickness of the manganese layer is variable but reaches 10 cm in some samples.

The five mineralized samples from Utu Sega are mainly composed of Mn oxides that form pale gray to dark gray stratiform layers with a submetallic to metallic luster (Fig. 4F). Three rock samples (FU-DR-22-02, FU-DR-22-04 and FU-DR-22-06) consist of alternating thin foraminiferous-rich beds and Mn oxide laminae with no or rare iron oxides. One of the mineralized rock sample (FU-DR-22-03) is also characterized by infilling of fractures by Mn oxides in strongly altered volcanic breccias. The manganese-rich samples collected at Utu Sega resemble the stratabound Mn described by Hein et al. (2008) from the Mariana and Izu-Bonin arc systems.

4.1.1. Mn oxide mineralogy and texture

XRD studies show that the Mn oxides mostly consist of a mixture of well-crystallized 7 Å (birnessite) and 10 Å (todorokite and/or "buserite") manganates. Vernadite (δ-MnO$_2$) may be present but the
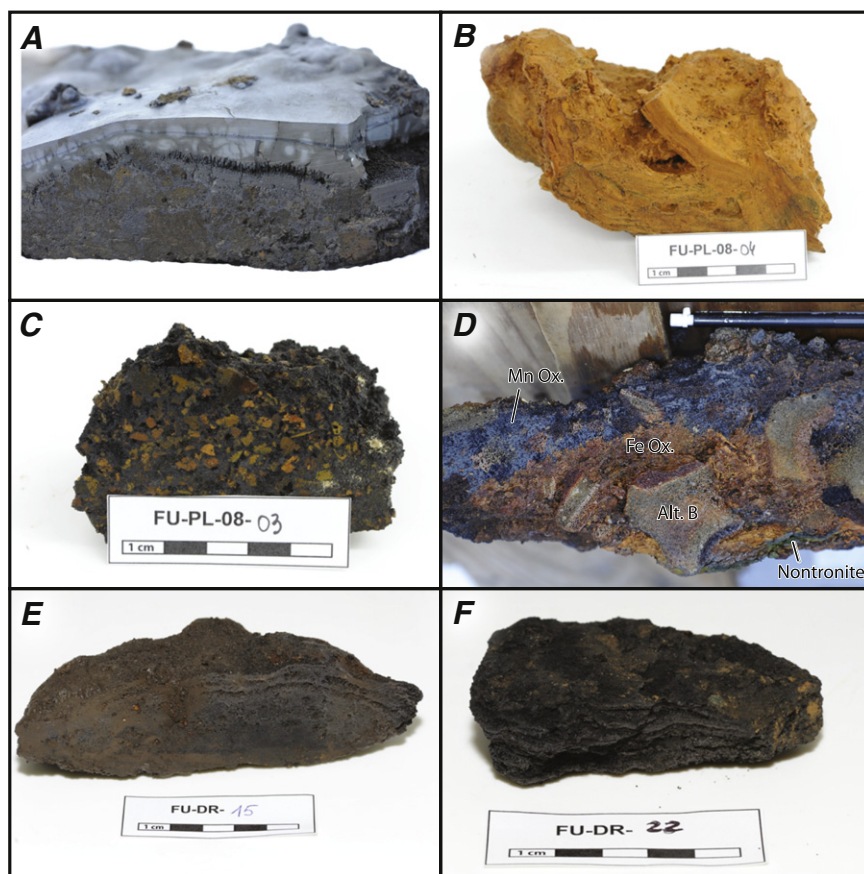
Fig. 4. A. Sample FU-DR01-03 (Utu Uli) composed of Mn-cemented breccia covered by a 2-cm-thick massive and layered Mn crust. B. Sample of an iron and silica-rich crest, which crosscuts the manganese mineralization at the surface (FU-PL08-04; Utu Uli). C. Mn oxide cemented pyroclastic breccia (FU-PL08-03; Utu Uli); pyroclasts are completely altered in a mixture of nontronite, Fe oxides and Mn oxides. D. Mn-Fe-Si cemented pyroclastic breccia displaying striking compositional layering; from top to bottom: Mn oxides, iron oxides and green nontronite; Alt. B: altered basaltic pyroclast. E. Stratabound Mn oxide sample (FU-DR15-10) characterized by a massive lower part and an upper part composed of alternating dense and porous layers. F. Stratabound Mn oxide bed composed of several metallic gray layers (FU-DR22-02; Utu Sega).

two X-ray diffraction reflections at ~2.46 Å and ~1.42 Å are overlapped by the XRD reflections of the birnessite and/or todorokite/"buserite". For this reason, vernadite is difficult to identify when accompanied by large proportion of 7 Å and/or 10 Å manganates. It is not possible to distinguish between todorokite and "buserite" using X-ray diffraction analyses alone since these two 10 Å manganates have similar X-ray diffraction reflections (Burns and Burns, 1977). The 10 Å interlayer spacing of "buserite" is known to collapse to the typical 7 Å birnessite spacing upon drying. In our samples, we cannot exclude a rapid collapse of the "buserite" upon drying before the first XRD analysis was performed at sea (~12 h after sampling). After three months, 10 Å manganates were clearly visible in more than half of the mineralized rocks. After five years, the transformation had progressed but 10 Å manganate was still detected in todorokite and/or "buserite"-rich samples. These observations suggest that two types of 10 Å manganate might exist in our samples: a mineral that collapses to 7 Å manganate over time and a manganate that does not collapse after drying.

Consequently, the relative proportions of well-crystallized 7 Å and 10 Å manganates in our samples, which reflect the qualitative assessment of diffractograms acquired three months after sampling, should be treated with caution.

A significant proportion of the Mn oxides found in the Utu Uli samples are 10 Å manganates (up to 65% of the manganates). The uppermost layered crust that outcrops at the seafloor-seawater interface displays the highest amount of 10 Å manganates, whereas the subsurface Mn oxides with breccia-like textures are dominated by birnessite. The Mn oxides found in Anakele samples are predominantly composed of 7 Å birnessite (89–100%) and the Mn samples collected at Utu Sega

show a high proportion of 10 Å manganates (36–82%) that were still present five years after sampling with no significant collapse to 7 Å Mn oxides.

From the study of polished sections and fragments of selected samples, two types of textures were distinguished: (i) massive and dense microcrystalline Mn oxides related to the precipitation of crust at the seafloor-seawater interface, and (ii) crystallization of Mn oxides in interstices of unconsolidated host rocks or, more rarely, fractures in volcanic breccias.

The first textural type (Fig. 5A) is characterized by dense homogeneous and laminated layers composed of microcrystalline Mn oxides. The manganates grew on unconsolidated pyroclastic rocks and are composed of botryoids that coalesce into densely packed layers with little pore space between them. SEM images of small fragments of crust (Fig. 6A) show a low porosity and a homogeneous crystallinity as revealed by the presence of small Mn oxides (≤1 μm).

The interstitial Mn oxides have a radial fibrous to spherulitic texture (Fig. 5B, C, D, E) that has sometimes coalesced to form scallop-like (Fig. 5F) and/or columnar (Fig. 6B) morphologies. Three mineral-size classes can be described: (i) amorphous cryptocrystalline oxides (AC), (ii) microcrystalline oxides (M) and (iii) crystalline oxides (C) (Fig. 6B, C, E). These classes are similar to those described by Hein et al. (2008) in stratabound Mn deposits from the Mariana and Izu-Bonin volcanic arcs. Individual spherules and radial fibrous structures are composed of alternating laminae of microcrystallites and crystallites and generally display an amorphous cryptocrystalline core (Fig. 5C, D and Fig. 6D). In stratabound Mn deposits (Hein et al., 2008), this alternation of AC, M and C oxides was interpreted as evidence for the waxing and waning
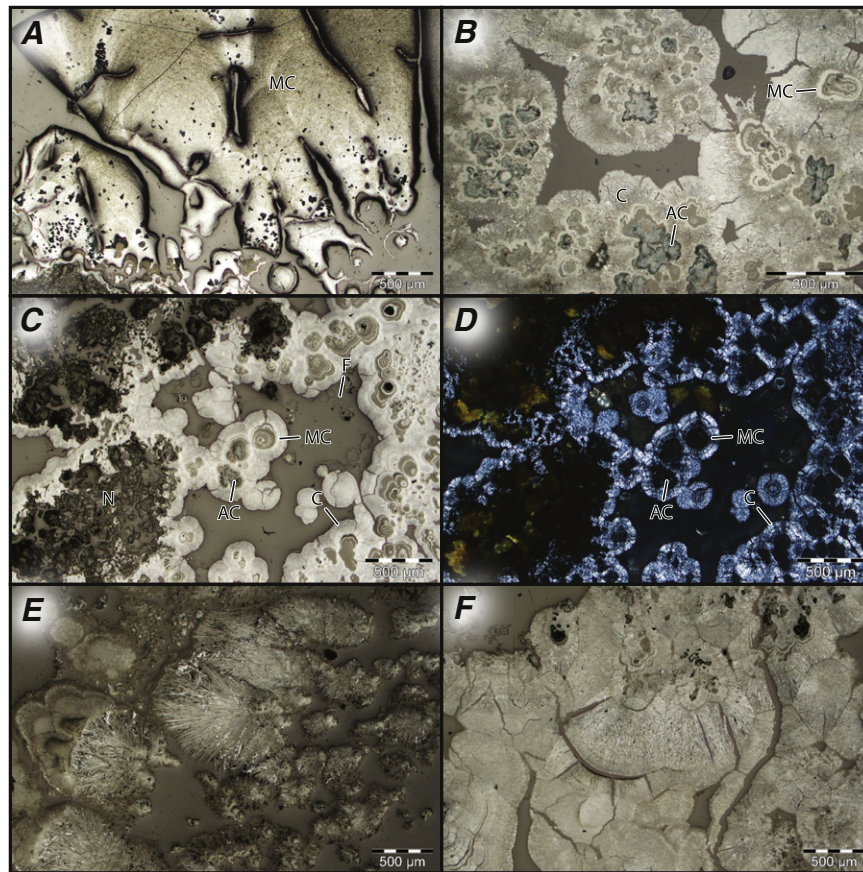
Fig. 5. Polished section photomicrographs. A. Dense Mn layer composed of laminated and coalescent botryoids (Layered Mn crust, FU-DR01-03). B. Radially oriented Mn oxides growing in open spaces and characterized by different mineral-size classes (Mn-cemented pyroclastic breccia, FU-DR01-03). C and D. Radial-fibrous and spherulitic Mn oxides growing in pore spaces and at the expense of nontronite clasts (Mn-cemented pyroclastic breccia, FU-DR01-03); reflected (Fig. 5C) and polarized reflected light (Fig. 5D). E. Radial-fibrous Mn oxides with crystallites up to 600 μm in size (Stratabound Mn oxide sample, FU-DR15-10). F. Scallop-like texture (Stratabound Mn oxide sample, Fu-DR22-03). AC: amorphous cryptocrystalline oxides; M: microcrystalline oxides; C: crystalline oxides.
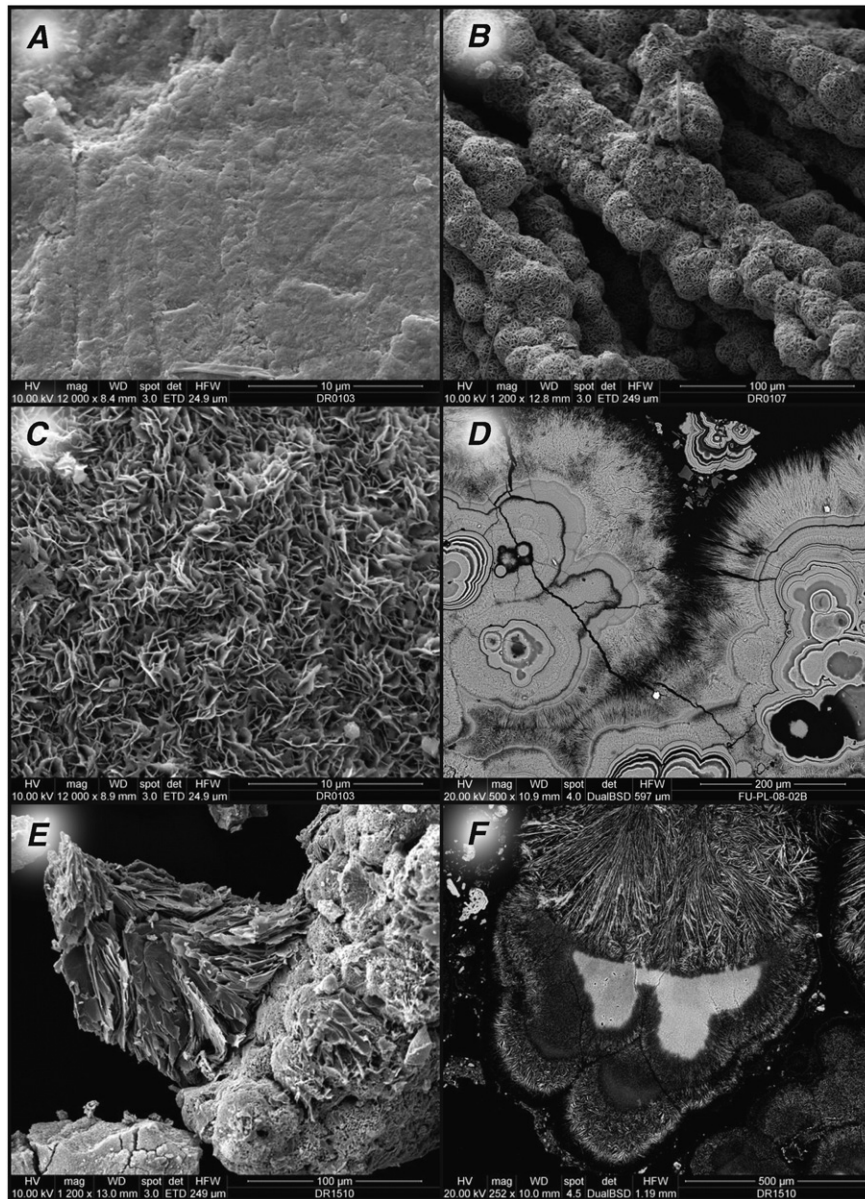
Fig. 6. Scanning electron microscope photomicrographs. A. Surface of the massive and dense layered Mn crust (FU-DR01-03). B. Coalescent botryoids forming a columnar-like structure (FU-DR01-07). C. Close-up of a well-crystallized botryoid composed of very thin blade-like crystals of manganates (FU-DR01-03). D. Backscattered electron image showing alternating layers of amorphous cryptocrystalline, microcrystalline and crystalline Mn oxides (FU-PL08-02). E. Secondary electron image of well-crystallized manganates (todorokite) with blade-like structure (FU-DR15-10). F. Backscattered electron image of large todorkite crystals underlying several Mn oxide botryoids; darker BSE signal of crystallites and microcrystallites in the botryoids is due to epoxy resin (FU-DR15-10).

stages of the hydrothermal fluid and mixing with oxygenated pore fluids, with the amorphous crytprocrystalline Mn oxides reflecting rapid precipitation (waxing stage) and the microcrystallites and crystallites (up to 600 µm in size at Anakele; Fig. 5E and Fig. 6E, F) suggestive of slower precipitation.

4.2. Sample geochemistry and growth rates

4.2.1. Bulk-rock composition

The chemical compositions of the Fe-Si-Mn mineralization are given in Table 1. Samples display a wide range of Fe/Mn ratios from nearly pure manganese oxides (e.g. FU-DR01-06: Mn = 52 wt.%; Fe < 0.7 wt.%) to Fe-Si-rich rocks with very low amount of Mn (e.g. FU-PL08-04: Mn < 0.8 wt.%; Fe = 37.1 wt.%; Si = 10.3 wt.%). The strong fractionation of iron and manganese is diagnostic of hydrothermal precipitates and is related to the different solubilities of iron and manganese oxides in hydrothermal fluids (Krauskopf, 1957). The aluminium

content is very low in all samples except three, which contain significant proportion of volcanogenic clasts (FU-PL08-02, FU-PL08-06 and FU-DR22-03). Aluminium correlates strongly with titanium (correlation coefficient: 0.983; Supplementary Table S1) and, to a lesser extent, with magnesium (0.743; Supplementary Table S1) and calcium (0.624; Supplementary Table S1) reflecting the association of these elements in the aluminosilicate component (e.g. pyroclastic rocks). However, the relatively high calcium concentrations in the Utu Sega mineralization reflect the presence of calcite. Except those with high aluminosilicate and/or carbonate components, most samples can be modeled using a three-component system with Mn oxyhydroxide, Fe oxyhydroxide and nontronite (Fig. 7). The strong negative correlation between the Mn content and the Fe (−0.938; Supplementary Table S1) and Si (−0.907; Supplementary Table S1) content as well as the good correlation between Fe and Si (0.751; Supplementary Table S1), reflects the striking mineralogical zoning (i.e. Mn oxides, Fe oxides and nontronite) that characterizes these deposits. Sodium is adsorbed to the surface of

Table 1

Chemical composition of bulk hydrothermal Fe-Mn-Si samples from Utu Uli, Anakele and Utu Sega.

Sample	FU-DR01-01	FU-DR01-03	FU-DR01-04	FU-DR01-06	FU-DR01-07	FU-DR01-08	FU-DR09-04	FU-DR09-06	FU-DR09-08	FU-DR09-09	FU-DR40	FU-PL08-01	FU-PL08-02
Type	Mn	Mn	Fe-Si-Mn	Mn	Mn	Mn	Fe-Si-Mn	Mn	Fe-Si	Fe-Si-Mn	Mn	Mn	Mn - alt. Bas
Localisation	Utu Uli	Utu Uli	Utu Uli	Utu Uli	Utu Uli	Utu Uli	Utu Uli	Utu Uli	Utu Uli	Utu Uli	Utu Uli	Utu Uli	Utu Uli
Fe/Mn	0.08	0.07	0.43	0.01	0.08	0.07	0.69	0.14	23.73	3.08	0.02	0.16	1.55
%													
Si	1.81	2.47	6.54	0.42	1.89	1.64	9.44	2.05	10.08	16.24	0.49	3.10	16.91
Al	0.44	0.12	0.42	0.12	0.18	0.19	0.80	0.27	0.20	0.28	0.15	0.56	5.68
Fe	3.40	3.11	11.59	0.65	3.49	3.21	16.10	5.52	36.79	24.11	0.83	5.53	12.08
Mn	42.46	45.22	27.09	52.05	44.37	43.10	23.23	39.12	1.55	7.82	48.76	35.49	7.79
Ca	0.83	1.78	1.02	0.83	1.00	0.77	1.06	1.20	1.64	0.81	0.99	1.27	3.89
Mg	1.20	0.58	1.53	1.03	1.06	1.03	1.26	1.55	0.85	1.40	1.21	1.98	2.82
K	0.63	0.35	0.71	0.83	0.76	0.71	1.06	0.77	0.32	1.19	0.72	0.95	1.24
Na	3.99	3.97	2.83	4.19	3.68	4.18	2.41	3.18	2.07	1.77	4.07	2.82	2.26
Ti	0.06	0.02	0.06	0.03	0.03	0.03	0.08	0.04	0.01	0.04	0.03	0.07	0.66
P	0.05	0.04	0.12	0.03	0.04	0.04	0.17	0.19	1.34	0.49	0.03	0.09	0.29
L.O.I. (110 °C)	12.32	8.40	13.01	6.64	6.97	7.42	10.97	8.28	N/A	11.43	3.74	15.36	7.64
L.O.I. (1050 °C)	16.46	15.92	15.89	16.04	16.40	16.56	12.98	17.69	11.45	10.10	16.39	17.61	7.92
ppm													
V	177	60	196	187	132	158	197	163	267	146	162	231	115
Co	1552	1510	494	2428	22,371	4431	5364	9881	454	2297	5692	154	88
Ni	46,129	1687	17,435	46,666	20,942	44,705	6122	16,627	540	2479	31,006	15,996	3993
Cu	200	41	115	249	1041	163	381	1813	150	703	227	418	66
Zn	206	–	113	135	54	120	61	227	38	56	288	752	90
As	31	17	80	14	31	26	64	46	224	85	20	47	50
Rb	6	4	12	6	6	6	21	5	5	26	4	7	17
Sr	260	320	263	284	288	226	266	408	569	295	296	328	349
Y	25	7	20	23	17	22	19	16	9	12	23	19	23
Zr	–	–	20	–	–	–	15	11	–	–	21	37	61
Ba	402	200	309	747	1070	468	1112	370	126	172	567	443	617
Mo	1386	1687	1124	1235	1086	1116	623	1841	20	382	1503	1141	180
Pb	10	–	12	–	–	–	8	34	11	8	–	18	–
Sb	22	6	6	10	9	5	5	24	9	–	46	35	7
Cd	11	–	3	3	4	6	3	10	N/A	3	19	17	–
Cs	44	43	30	42	44	35	24	36	N/A	5	45	34	11
Tl	22	–	11	–	–	8	–	55	–		20	67	
Co + Ni + Cu (%)	4.79	0.32	1.80	4.93	4.44	4.93	1.19	2.83	0.11	0.55	3.69	1.66	0.41

Table 1 (*continued*)

FU-PL08-03	FU-PL08-04	FU-PL08-05	FU-PL08-06	FU-PL09-01	FU-PL09-02	FU-PL09-03	FU-DR15-05	FU-DR15-06	FU-DR15-07	FU-DR15-09
Fe-Mn-Si	Fe-Si	Fe-Mn-Si	Mn - alt. Bas	Fe-Mn-Si	Fe-Si	Fe-Mn-Si	Mn	Fe-Si-Mn	Fe-Si	Fe-Si-Mn
Utu Uli	Utu Uli	Utu Uli	Utu Uli	Utu Uli	Utu Uli	Utu Uli	Anakele	Anakele	Anakele	Anakele
0.64	47.79	3.81	0.39	2.67	20.87	0.48	0.07	0.64	15.63	0.43
%										
8.55	10.34	12.15	8.00	3.64	15.56	8.76	1.70	5.98	19.13	6.35
0.58	0.44	0.22	3.89	0.20	0.17	0.73	0.15	0.87	0.97	0.82
15.16	37.12	28.01	8.02	35.40	30.29	12.08	2.86	16.51	27.55	12.03
23.53	0.78	7.35	20.79	13.27	1.45	25.15	39.78	25.82	1.76	27.95
1.70	1.63	0.88	4.55	0.76	1.13	1.76	1.29	1.44	0.70	1.22
1.71	0.73	1.32	2.90	0.87	0.83	2.47	1.52	1.70	1.38	1.65
0.80	0.27	0.63	0.66	0.51	0.53	0.99	0.85	0.85	0.60	0.99
2.41	2.31	1.92	1.95	1.77	2.27	2.08	2.88	2.18	1.76	2.28
0.10	0.05	0.04	0.52	0.05	0.01	0.14	0.02	0.11	0.07	0.06
0.17	0.95	0.52	0.25	1.02	1.68	0.13	0.05	0.19	0.25	0.11
7.01	N/A	15.56	13.38	8.36	N/A	6.07	9.14	6.80	N/A	6.70
16.03	12.81	11.93	14.77	14.99	10.36	14.91	17.85	16.43	8.61	16.02
ppm										
326	110	354	369	1795	315	303	319	507	316	289
1956	309	2237	2291	4856	208	978	13,267	488	509	1309
16,006	289	3455	3399	4929	599	8884	7866	10,184	785	6380
448	26	249	5567	812	39	135	15,329	2013	781	11,650
616	33	142	630	254	52	300	414	724	169	468
119	179	239	141	697	204	100	43	129	122	65
10	8	14	6	3	8	13	7	9	13	10
344	519	287	522	359	480	370	417	436	145	305
23	7	14	40	86	39	18	19	41	30	15
57	–	15	87	44	–	25	–	103	27	29
356	70	200	721	922	101	585	1296	756	231	785
520	15	252	567	752	67	458	1236	702	60	490
43	14	9	122	47	11	15	–	93	24	15
43	N/A	6	62	28	–	55	115	53	8	39
23	N/A	–	18	–	N/A	–	16	17	N/A	10
23	N/A	5	24	9	N/A	28	40	27	N/A	28
105	8	78	31			19	26	65		39
1.84	0.06	0.59	1.13	1.06	0.08	1.00	3.65	1.27	0.21	1.93

Table 1 (*continued*)

| FU-PL09-03	FU-DR15-10	FU-DR15-11	FU-PL10-04	FU-PL10-06	FU-PL10-07	FU-DR22-02	FU-DR22-03	FU-DR22-04	FU-DR22-05	FU-DR22-06
Fe-Mn-Si	Mn	Fe-Si	Fe-Mn-Si	Fe-Mn-Si	Fe-Mn-Si	Mn - sed.	Mn - sed. - bas	Mn - sed.	Mn	Mn - sed.
Utu Uli	Anakele	Anakele	Anakele	Anakele	Anakele	Dorsale Alofi	Dorsale Alofi	Dorsale Alofi	Dorsale Alofi	Dorsale Alofi
0.48	0.08	36.32	6.69	9.78	2.22	0.00	0.05	0.01	0.00	0.01
%										
8.76	1.68	18.32	12.96	10.17	11.96	0.34	8.05	0.80	0.11	0.72
0.73	0.21	0.21	0.48	1.25	0.62	0.45	2.62	0.71	0.35	0.67
12.08	3.50	30.15	31.91	31.40	23.09	0.21	1.69	0.32	0.21	0.57
25.15	42.09	0.83	4.77	3.21	10.39	50.48	36.01	46.90	48.16	44.55
1.76	1.11	0.75	0.70	2.29	0.93	2.69	5.76	4.31	1.46	5.52
2.47	1.28	1.19	1.17	0.95	1.45	1.79	2.63	1.64	1.78	1.47
0.99	0.78	0.44	0.50	0.53	0.77	0.68	0.46	0.38	0.66	0.32
2.08	3.52	2.02	1.56	2.66	1.99	3.14	2.94	3.30	3.33	3.32
0.14	0.03	0.01	0.05	0.09	0.05	0.03	0.29	0.05	0.01	0.04
0.13	0.04	0.47	0.37	1.00	0.42	0.02	0.04	0.03	0.02	0.03
6.07	9.69	N/A	8.58	N/A	10.71	13.96	8.12	19.29	21.99	17.28
14.91	17.23	9.18	10.66	14.34	11.90	16.82	14.61	17.74	17.76	18.32
ppm										
303	218	181	706	469	345	392	360	462	429	429
978	9040	111	1398	628	596	9686	6800	12,304	8331	11,254
8884	6297	90	1167	1199	1591	2909	1297	2298	6569	2175
135	15,305	72	2954	1910	1895	4333	3066	4806	4933	4475
300	256	83	171	237	133	118	91	112	506	97
100	21	118	199	232	192	9	6	12	9	14
13	6	8	9	10	9	4	3	3	3	3
370	268	252	240	404	237	346	309	357	352	414
18	9	23	28	43	30	10	12	15	15	17
25	–	–	24	91	19	–	19	–	–	–
585	880	107	400	287	649	345	142	503	307	301
458	545	52	119	109	325	615	460	494	606	487
15	–	12	15	30	7	–	–	–	8	–
55	122	–	14	N/A	24	49	28	57	131	42
–	16	N/A	19	N/A	3	20	5	N/A	30	11
28	42	N/A	–	N/A	7	48	40	38	41	43
19	25					14	40	47	316	41
1.00	3.06	0.03	0.55	0.37	0.41	1.69	1.12	1.94	1.98	**1.79**
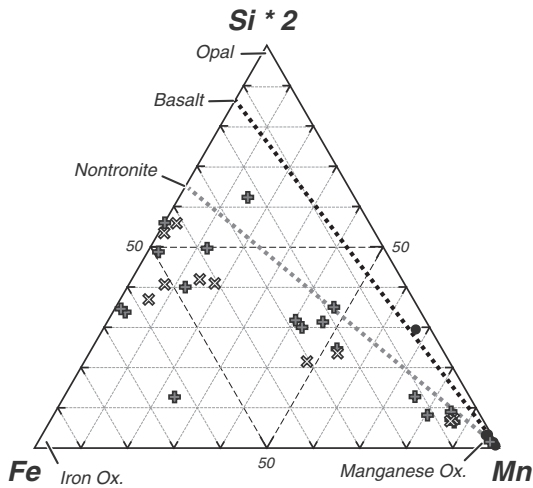
Fig. 7. Fe-Mn-(Si)×2 ternary diagram showing the composition of ferromanganese precipitates from Utu Uli (dark gray crosses), Anakele (light gray crosses) and Utu Sega (black circles); the gray dotted line represents mixing between pure Mn oxide and an ideal nontronite composition; the black dotted line represents a mixing line between pure Mn oxide and the mean basalt composition of the study area.

Mn oxides (Na and Mn: 0.843; Supplementary Table S1) whereas phosphates is scavenged by Fe oxides (P and Fe: 0.821; Supplementary Table S1).

Metals such as Ni, Cu, Co and Mo are unexpectedly enriched for a Fe-Si-Mn mineralization that precipitated from a hydrothermal process. Nickel, cobalt, copper and molybdenum in the manganese-rich samples (i.e. >35 wt.% Mn) range from 0.13 to 4.67 wt.%, 0.01 to 2.24 wt.%, 41 ppm to 1.53 wt.% and 0.05 to 0.18 wt.%, respectively. In details, there are strong differences in Ni, Co and Cu enrichment between the three deposits (Fig. 8A): Mn oxides are usually enriched in nickel at Utu Uli (Mn-Ni correlation: 0.777; Supplementary Table S3), copper at Anakele (Mn-Ni correlation: 0.905; Supplementary Table S4) and cobalt at Utu Sega. The highest metal concentrations are recorded in the purest Mn oxide samples (Fig. 8B, C, D, E, F). The only exception to this is for samples that exhibit the mineralogical and textural characteristics of Mn precipitates formed in contact with seawater (i.e. layered crust and Fe-Si ± Mn crests; e.g. FU-DR01-03, FU-PL10-08 and FU-DR15-11). The positive correlation observed between the sum of selected metals (i.e. Ni, Co and Cu) and Mn (Fig. 8B; Supplementary Table S2) is consistent with adsorption of metals by Mn oxyhydroxides (Post, 1999).

Barium is also high in some of the Mn oxide samples (up to 1296 ppm) but displays lower mean concentrations compared to the Mn-stratabound mineralization analyzed by Hein et al. (2008, 1996) and González et al. (2016).

Total Rare Earth Elements (REE) abundances (Table 2) are low (12–121 ppm), consistent with the hydrothermal signature; if one outlier is not considered (FU-DR15-06; Anakele), the REE content would range from 12 to 41 ppm. The chondrite-normalized patterns (Sun and McDonough, 1989) of the Utu Uli and Anakele samples are similar to the pattern for seawater (Fig. 9A, B) with light-REE enrichment and a negative Ce anomaly (Ce/Ce*: 0.04–0.49). At Utu Sega, the Mn precipitates show a distinctive signature with low light-REE concentrations (Fig. 9C), negative to positive Ce anomaly (Ce/Ce*: 0.47–1.47) and a positive Eu anomaly (Eu/Eu*: 1.18–1.72). In deep-sea environments, a positive europium anomaly is diagnostic of reduced, chlorine-rich hydrothermal fluids (e.g. Craddock et al., 2010; Douville et al., 1999; Michard, 1989; Michard and Albarède, 1986).

4.2.2. Classification of the mineralization

On the basis of the (Co + Ni + Cu)× 10-Fe-Mn ternary diagram (Bonatti et al., 1972; Toth, 1980), most of the Wallis and Futuna back-arc samples fall within two fields: (i) the hydrothermal and (ii) the hydrogenetic field (Fig. 10). The iron-silica rich samples plot in the hydrothermal field whereas samples with significant amount of Mn oxides fall within the hydrogenetic field. However, the purest Mn oxides samples of Utu Uli and Anakele plot outside of the three fields defined by Bonatti et al. (1972) owing to the unusually high metals concentrations. One exception is sample FU-DR01–03 which is classified as hydrothermal in the ternary diagram. This sample has a large proportion of the massive and laminated crust that precipitates directly on the seafloor. The Mn oxides samples of Utu Sega can be distinguished from others since they fall within the upper limit or outside the diagenetic field. In order to discriminate Mn oxides, other discrimination diagrams have been tested (Supplementary Fig. S1; Bau et al., 2014; Choi and Hariya, 1992; Dymond et al., 1984; Nicholson, 1992; Toth, 1980). They generally fall within two or three fields (i.e. hydrothermal, hydrogenetic, diagenetic) and sometimes outside defined fields. Basically, diagrams based on REE favor a hydrothermal origin whereas the diagrams based on transition metals point to a diagenetic or hydrogenetic origin. As proposed in previous study using discrimination diagrams based on transition metals (e.g. Conly et al., 2011; González et al., 2016; Hein et al., 2008), the samples that fall outside the hydrothermal field must not be considered definitively as "not hydrothermal". Instead, this should be viewed as the result of the extreme enrichment of Ni, Co and Cu.

4.2.3. Growth rate estimations

Because of the extreme enrichment of cobalt in most of the precipitates studied here, growth rates were not determined using the empirical equation of Manheim and Lanebostwick (1988) which is based on normalized Co concentrations. Use of this equation would lead to growth rates as low as 0.16 mm/Ma which is unlikely even for hydrogenetic crust. Such abnormal growth rates might reflect a large contribution of hydrothermally-derived cobalt. Since REE are expected to be low in deep-sea hydrothermal fluids (Douville et al., 2002) and as the hydrothermal REE contribution can be traced by the presence of Eu positive anomaly, an alternative to the Co-flux model that could be used is the Ce_{xs} model (Kuhn et al., 1998). The Ce_{xs} is a parameter that quantifies the degree of decoupling of Ce from other REE and is related to the growth rate. Following the empirical equation of Kuhn et al. (1998), the growth rate (mm·Ma^{-1}) is given by:

$$GR = \frac{1.94 * 10^4}{Ce_{xs}^{1.43}}$$

where $Ce_{xs} = Ce_{Fe-Mn\ crust} - \left[\frac{Ce_{sw} Pr_{Fe-Mn\ crust}}{Pr_{sw}}\right]$

and $Ce_{Fe-Mn\ crust}$ and $Pr_{Fe-Mn\ crust}$ are the Ce and Pr concentrations, respectively, in the Fe-Mn crust, and $Ce_{sw\ and}$ Pr_{sw} are the Ce and Pr concentrations in seawater.

Using this method, the Utu Uli Mn oxides have the highest meangrowth rates, with four samples yielding rates over 9000 mm/Ma. One sample is characterized by a very high growth rate of over 500,000 mm/Ma, and two samples have rates of <4500 mm/Ma. At Anakele, the growth rates of manganese samples range from 240 to 6716 mm/Ma. One sample (FU-DR10-06; Table 3) yields a low rate of 240 mm/Ma. Since this sample is characterized by the highest total REE concentrations, the low growth rate might indicate a slight hydrogenetic component. The Utu Sega Mn oxide samples have growth rates ranging from 1719 to 144,408 mm/Ma. These might represent minimum growth rates for the Utu Sega sample as the presence of a positive Eu anomaly in REE patterns indicates a hydrothermally-derived REE contribution. Moreover, the REE contribution from volcanic components (FU-DR22-03; Al = 2.62 wt.%)may explain the lowest growth rate estimate at Utu Sega (i.e. 1719 mm/Ma). Overall, the estimated growth rates are fairly typical of hydrothermal Mn oxides (Hein et al., 2008). By
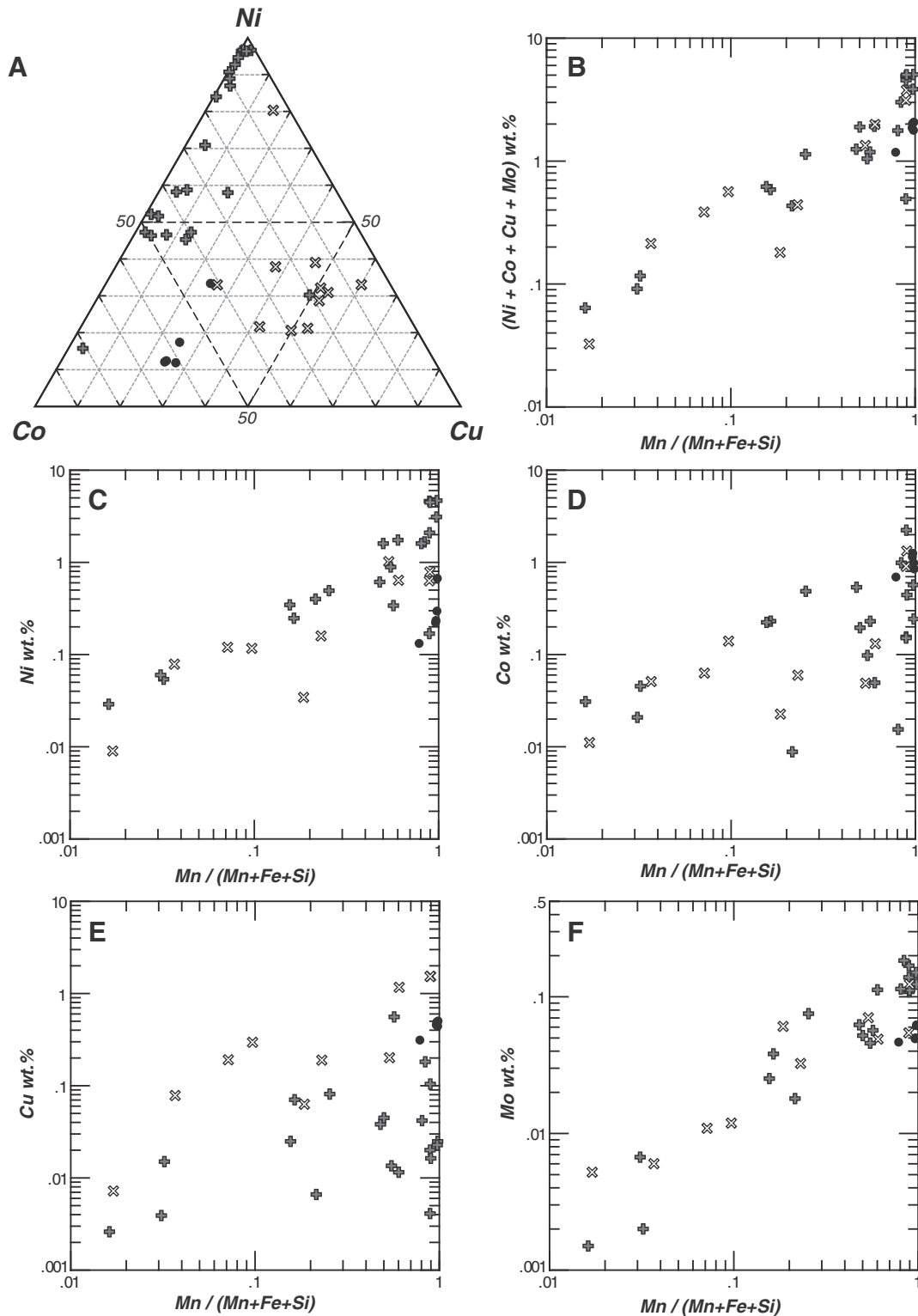
Fig. 8. A. Co-Ni-Cu ternary diagram showing the compositional difference in trace metals in the Mn deposits. B. Mn / (Mn + Fe + Si) versus Ni + Co + Cu concentrations (in wt.%). C. Mn / (Mn + Fe + Si) versus Ni concentratins (in wt.%); At Utu Uli, the nickel content is clearly controlled by the manganates. D. Mn/(Mn + Fe + Si) versus Co concentrations (in wt.%); several mineralized samples at Utu Uli and Anakele support some degree of affinity between Co and manganates; at Utu Sega, the Co content is clearly controlled by the manganates. E. Mn / (Mn + Fe + Si) versus Cu concentrations (in wt.%); only the Anakele samples show a significant correlation between Cu and high Mn concentrations. F. Mn / (Mn + Fe + Si) versus Cu concentrations (in wt.%). Same legend as Fig. 7.

dividing the maximum thickness of the manganese mineralization (~10 cm) by the mean growth rates, a precipitation duration of around 1000–30,000 years is estimated. However,this does not take into account possible dissolution-reprecipitation processes that might have occurred during successive hydrothermal episodes.

4.2.4. Electron microprobe composition of manganese oxyhydroxides

Overall, the Mn oxides have high Mn contents (>30 wt.%) and low Fe contents (<2 wt.%) (Table 3). The relatively high amount of manganese, particularly in AC oxides, points to a small proportion of adsorbed water and a low porosity of the Mn oxides. The massive layered crust that has

Table 2
Rare earth elements composition of 15 hydrothermal Mn samples.

Sample	Site	Nature	La	Ce	Pr	Nd	Sm	Eu	Gd	Tb	Dy	Ho	Er	Yb	Lu	ΣREE	Ce/Ce*	Eu/Eu*	Ce$_{xs}$	GR (mm.Ma^{-1})
FU-DR01-01	Utu Uli	Mn	10.13	2.45	1.84	8.39	1.48	0.47	2.18	0.34	2.41	0.63	1.88	1.67	0.28	34.2	0.14	0.79	1.60	9936
FU-DR01-03	Utu Uli	Mn	3.61	1.35	0.59	2.60	0.49	0.14	0.72	0.12	0.88	0.22	0.71	0.61	0.09	12.1	0.23	0.70	1.08	17320
FU-DR01-04	Utu Uli	Fe-Si-Mn	7.79	4.11	1.20	5.50	1.07	0.31	1.66	0.27	1.93	0.50	1.59	1.50	0.24	27.6	0.33	0.70	3.55	3167
FU-DR01-06	Utu Uli	Mn	13.49	0.87	1.65	7.56	1.20	0.37	2.11	0.33	2.51	0.70	2.21	1.93	0.32	35.2	0.04	0.71	0.10	514256
FU-DR01-07	Utu Uli	Mn	10.84	1.94	1.55	6.96	1.13	0.31	1.61	0.24	1.73	0.47	1.46	1.15	0.19	29.6	0.11	0.69	1.23	14501
FU-DR01-08	Utu Uli	Mn	3.53	3.25	0.74	3.40	0.74	0.27	1.10	0.17	1.31	0.84	0.80	0.13	16.4	0.49	0.90	2.91	4206
FU-DR15-05	Anakele	Mn	11.61	5.10	1.74	8.01	1.64	0.48	2.79	0.45	3.14	0.79	2.41	2.45	0.42	41.0	0.27	0.69	4.29	2417
FU-DR15-06	Anakele	Fe-Si-Mn	32.68	24.26	5.76	25.34	5.20	1.38	6.81	1.09	7.06	1.61	4.78	4.61	0.72	121.3	0.43	0.71	21.59	240
FU-DR15-09	Anakele	Fe-Si-Mn	8.32	6.90	1.84	8.21	1.64	0.44	2.23	0.35	2.40	0.62	1.93	1.88	0.32	37.1	0.43	0.70	6.05	1479
FU-DR15-10	Anakele	Mn	5.17	2.66	1.21	5.39	1.01	0.27	1.51	0.23	1.63	0.46	1.47	1.39	0.25	22.7	0.26	0.66	2.10	6716
FU-DR22-02	Utu Sega	Mn	1.11	1.36	0.28	1.50	0.46	0.31	0.90	0.20	1.73	0.50	1.78	2.06	0.36	12.6	0.59	1.48	1.23	14408
FU-DR22-03	Utu Sega	Mn - alt. Bas	1.50	5.72	0.59	3.24	1.13	0.55	1.77	0.35	2.57	0.62	1.94	1.98	0.32	22.3	1.47	1.18	5.45	1719
FU-DR22-04	Utu Sega	Mn	1.73	4.60	0.47	2.54	0.82	0.57	1.53	0.34	2.91	0.82	2.85	3.19	0.55	22.9	1.23	1.56	4.38	2345
FU-DR22-05	Utu Sega	Mn	1.64	1.63	0.44	2.64	0.95	0.79	2.05	0.47	4.03	1.11	3.51	3.56	0.60	23.4	0.47	1.72	1.43	11625
FU-DR22-06	Utu Sega	Mn	2.02	4.61	0.55	2.84	0.87	0.57	1.59	0.34	2.86	0.79	2.69	2.99	0.52	23.2	1.06	1.47	4.36	2361

Ce/Ce*: $\frac{Ce}{Ce^*} = \frac{Ce_n}{\sqrt{(La_n.Pr_n)}}$; Eu/Eu*: $\frac{Eu}{Eu^*} = \frac{Eu_n}{\sqrt{(Sm_n.Gd_n)}}$.

Ce$_{xs}$: Cerium excess; GR: Growth rates in mm·Ma^{-1}.

precipitated on the seafloor has lower Mg and higher Na than Mn oxides that formed underneath the crust. High sodium content in Mn oxides is typical of seafloor or near seafloor deposition. In addition, a low magnesium content might be indicative of its removal by clay minerals (e.g. nontronite) during hydrothermal alteration of basaltic rocks (Hein et al., 2008).

The chemical maps show that Ni, Co and Cu concentrations are systematically very low in the layered massive crust (Fig. 11A) but high (several percent) in the Mn oxides cement (Fig. 11B, C; Table 3). In Fig. 11B, the highest nickel concentrations seem to be confined to area close to the nontronite clasts, however the effect of either high porosity or epoxy resin dilution on the relative Ni depletion observed locally cannot be ruled out. Nevertheless, the progressive depletions in Fe and Si and enrichments in Mn and Ni in the nontronite likely indicates its progressive replacement. Furthermore, the high Fe and Si in the manganates at the Mn oxide-clay transition zone might suggest the presence of residual nontronite.

EMP spot analyses and chemical maps show that, in general, Mn, Na and K increase with increasing crystallinity (Table 3). In contrast, Fe, Si, Mg, Al and Ca all decrease with increasing crystallinity. AC Mn oxides have higher mean concentrations of Co than MC and C Mn oxides (Table 3). High nickel and copper contents were recorded in the three mineral-size classes; however the AC oxides have lower nickel contents than the microcrystallites (MC). It is clear from the EMP chemical maps (Fig. 11C) that cobalt, nickel and copper are decoupled. However, cobalt is clearly not restricted to the AC core and is sometimes higher in crystallites (Fig. 11C). Areas where Co is enriched, correspond to areas where nickel is systematically depleted and vice versa. Copper appears to mostly follow nickel, though its behavior is somewhat transitional between Co and Ni.

5. Discussion

5.1. Origin of Fe-Si-Mn precipitates of the Wallis and Futuna back-arc system

Given its location at the axis of the northern edge of the Futuna spreading center, the Utu Uli deposit is probably the youngest of the three deposits. At Anakele, the volcanic edifice is located approximately 20 km east of the Futuna spreading center. Given the spreading rate of 4 cm/yr (Pelletier et al., 2001), the volcanic rocks might be as young as 500,000 yrs here. However, the presence of a 1-cm-thick hydrogenetic crust (2010 sample description by Fouquet et al., (unpublished data, 2010)) indicates that the main volcanic edifice could be significantly older (a few Ma in age). The age of the Mn oxides collected at Utu Sega is difficult to estimate as we have little information on the local

geology (no submersible dive was performed here). Given its location 20 km west of the axis of the Alofi spreading center and assuming a similar spreading rate to the Futuna ridge, the maximum age should be <1 Ma.

In-situ observations of ridges and crests at the surface of the deposit, the increasing of thickness of the mineralization towards the top, and the mineralogical and textural evidence, all suggest that the Fe-Si-Mn precipitates formed from hydrothermal fluids circulating through a volcanic basement. The high Fe or Mn content and the large degree Fe/Mn fractionation also support a hydrothermal origin for the deposits. The pure iron-silica samples exhibit low metal contents (Fig. 8), as would be expected for hydrothermal precipitates. Conversely, the concentrations of nickel, cobalt and copper in the mixed iron-silica-manganese samples are comparable to those reported for hydrogenetic crusts (Fig. 8, Table 4). Several Mn-rich samples exhibit Ni + Cu + Co contents that exceed 4.9 wt.% (Table 1). To the best of our knowledge, these represent the highest base metals concentrations ever recorded for a bulk sample of deep-sea ferromanganese rock. However, the Mn oxide could not have formed by hydrogenetic or diagenetic processes because the time required to develop the precipitates is much longer (10 cm: > 10 Ma; (Hein et al., 2000)) than the estimated age of the deposits (see discussion above). The total REE concentrations, estimated growth rates, and chondrites-normalized REE patterns definitively ruled out a major hydrogenetic or diagenetic influence for the three deposits.

Several authors (e.g. Conly et al., 2011; González et al., 2016; Hein et al., 2008; Hein et al., 1996; Hein et al., 1992; Hein et al., 1990) have suggested that the metal enrichment should be used with caution when trying to decipher the processes involved in the formation of Fe-Mn mineralization. It is clear that the extreme and generalized Ni, Co, and Cu enrichments that we report for our hydrothermal Mn ± Fe ± Si precipitates could give misleading information on the origin (hydrogenetic, diagenetic or hydrothermal) of the mineralization. This is particularly true when using the classical conventional discrimination diagrams, which are mostly based on transition metals concentrations (Bonatti et al., 1972; Choi and Hariya, 1992; Nicholson, 1992; Toth, 1980).

Concentrations of the so-called immobile elements (e.g. Ti, Zr, Y, REE), which are expected to be low in acidic, chlorine-rich hydrothermal fluids (Douville et al., 2002), are also low in our samples. Thus, as proposed by Bau et al. (2014) and Josso et al. (2016), the metal-rich hydrothermal Mn oxides might be best discriminated using these trace elements.

5.2. Source(s) of the metals

Clearly, the metals enrichment reported in our samples (Ni, Co, Cu) make the Utu Uli, Anakele and Utu Sega deposits rather unusual.
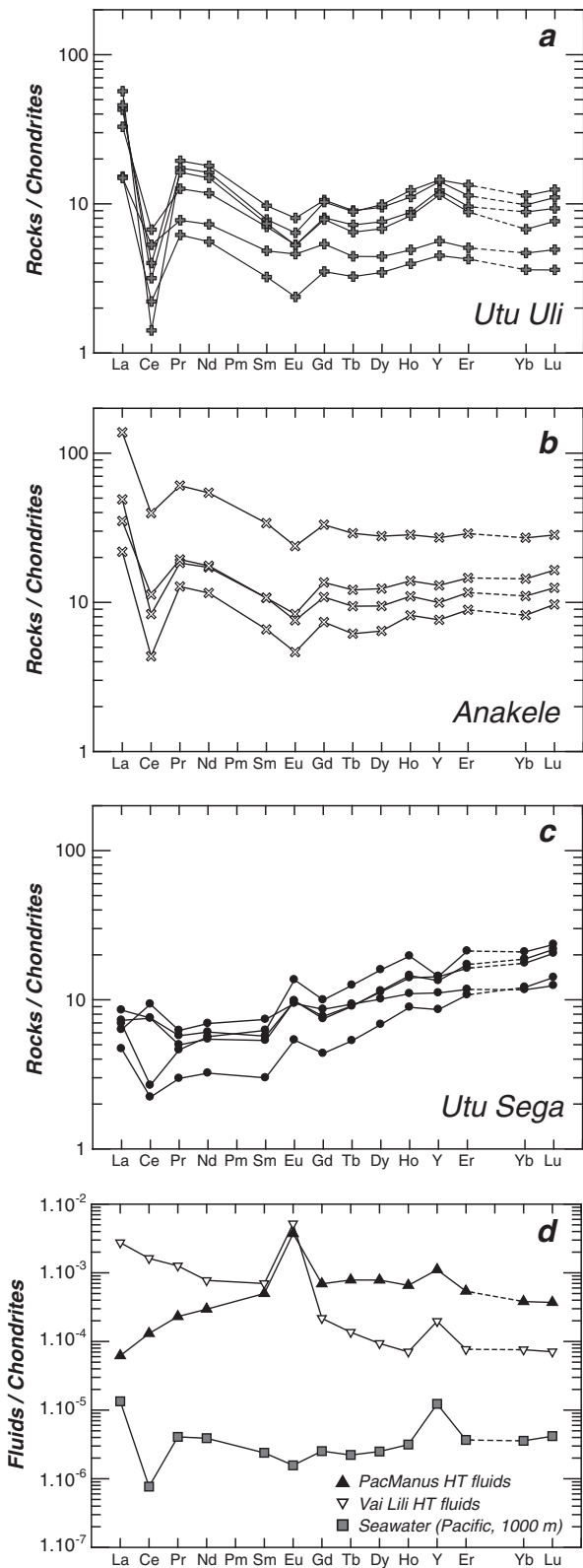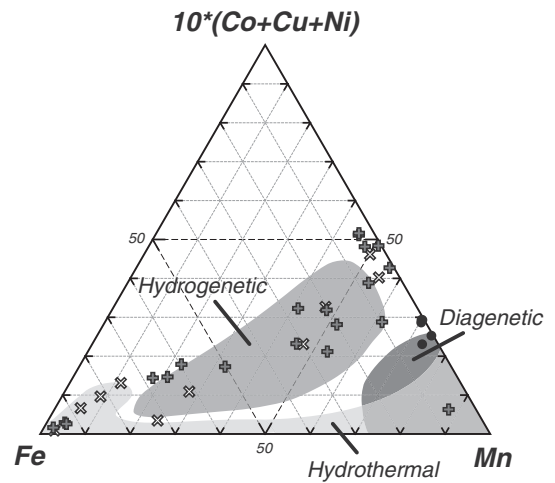
Fig. 10. Fe-Mn-(Co + Ni + Cu)×10 ternary diagram (Bonatti et al. 1972); same legend as Fig. 7.

the Ni, Co, and Cu concentrations were typically more than one order of magnitude lower than those of the deposits studied here (Table 4). Different source components were proposed to explain the large chemical variations in trace elements such as Mo, Ni, Cr, Cu, Zn, Co, Pb or Ba. For example, the leaching of ultramafic rocks was invoked to explain high Ni (up to 0.58 wt.%) and Cr (up to 0.15 wt.%) concentrations in the stratabound Mn samples from the Yap arc (Hein et al., 1992). Other sources that have been invoked include the leaching of igneous rocks of different compositions, sulfide mineralization, biogenic sediments and/or the addition of metals from seawater (e.g. González et al., 2016; Hein et al., 2008; Hein et al., 1996; Hein et al., 1990; Kuhn et al., 2003; Moorby et al., 1984; Rogers et al., 2001). As discussed earlier (see Section 5.1), a major seawater contributions for Ni, Co and Cu can be ruled out by the geological setting, the textural and mineralogical features, the fast precipitation of Mn oxides or the lack of correlations between these metals and elements commonly enriched by a hydrogenetic process (e.g. REE, Ti, Zr). Chromium concentrations in the Ni-rich Mn oxides analyzed by electron microprobe were systematically below the detection limit (i.e. <500 ppm). The absence of chromium anomalies, even in Mn oxides with up to 5 wt.% Ni seems to preclude an ultramafic origin for the nickel (Hein et al., 2008). Furthermore, except for in a deep fault located east of Alofi island, no ultramafic rocks exposures were identified in the Futuna area. A remobilization of massive sulfide bodies by the hydrothermal fluids that precipitated the Mn oxides is also unlikely given the low Zn, Cd and Pb concentrations (Table 4) and the fact that Cu and Co does not correlate with Zn in the Mn oxides samples. In addition, typical sulfide deposits associated with basaltic rocks are not enriched in Ni (Fouquet et al., 2010). The mean concentrations of calcium and barium in the Utu Uli and Anakele samples are lower than those reported for the Valu Fa Ridge, the Mariana, Izu Bonin, Tonga and Yap arc and the Hawaiian rift zone (Table 4) (Hein et al., 1997). The high calcium contents in the Utu Sega Mn oxide samples are related to the presence of calcite rather than to significant Ca enrichment in Mn oxides. Electron microprobe analyses confirm the relatively low calcium concentration in the Mn oxides (Table 3). Consequently, biogenic sediments are unlikely to have contributed significantly to the Ni, Cu- and Co-rich compositions of the Mn oxides. Relatively low Ba and Sr concentrations also support the minimal sediment influence, although these might also reflect the precipitation of barite at depth.

Together, these different lines of evidence favor a volcanic source for the Ni, Co and Cu rather than leaching of massive sulfides, ultramafic rocks or biogenic sediments.

Molybdenum contents are similar to other Mo-rich hydrothermal Mn precipitates (e.g. Hein et al., 2008, Hein et al., 1990; Krasnov et al., 1995; Kuhn et al., 2003; Moorby et al., 1984; T. D. S. Rogers et al.,

Fig. 9. Chondrite-normalized (Sun and McDonough, 1989) REE plots for Mn oxides from (a) Utu Uli, (b) Anakele, (c) Utu Sega; (d) REE patterns of Pacific seawater (1000 mbsl; Alibo and Nozaki, 1999) and selected Pacific HT hydrothermal fluids (PacManus and Vai Laili; Douville et al., 1999).

Relatively high trace metal have also been reported for stratabound hydrothermal Mn deposits in other tectonic settings (e.g. González et al., 2016; Hein et al., 2008; Hein et al., 1996; Kuhn et al., 2003), though

Table 3
Selected electron microprobe spot analyses of Mn oxides (CAMECA SX100, Microsonde Ouest, Brest).

Sample	Site	Nature	Mn	Fe	Si	Al	Mg	Na	K	Ca	Co	Cu	Ni	P
FU-DR01-03	Utu Uli	C	51.60	0.09	0.04	–	0.92	3.36	0.94	1.44	0.33	–	0.54	–
FU-DR01-03	Utu Uli	C	49.48	0.68	0.80	0.34	2.17	3.11	0.33	1.24	–	–	1.37	–
FU-PL08-06	Utu Uli	C	51.38	0.18	0.10	0.56	2.27	1.95	1.06	1.30	0.28	2.37	0.38	–
FU-DR15-10	Anakele	C	49.39	–	0.10	0.20	2.89	1.78	1.53	0.64	2.50	0.35	0.31	–
FU-DR15-10	Anakele	C	53.06	–	–	0.22	0.73	4.17	0.59	1.25	1.12	0.73	–	–
FU-DR15-10	Anakele	C	45.76	–	–	0.09	0.40	3.84	0.41	0.88	1.25	2.29	0.62	–
FU-DR22-03	Utu Sega	C	55.66	0.10	0.09	0.16	0.71	4.30	0.57	1.27	0.19	0.33	–	–
FU-DR22-03	Utu Sega	C	50.42	–	0.06	0.28	0.58	3.24	0.23	1.05	0.35	0.32	–	–
FU-DR22-03	Utu Sega	C	50.79	0.09	0.05	0.31	1.04	3.73	0.21	1.19	0.61	0.65	0.27	–
Mean			50.84	0.23	0.18	0.27	1.30	3.28	0.65	1.14	0.83	1.00	0.58	
Maximum			55.66	0.68	0.80	0.56	2.89	4.30	1.53	1.44	2.50	2.37	1.37	
Minimum			45.76	0.09	0.04	0.09	0.40	1.78	0.21	0.64	0.19	0.32	0.27	
SD			2.72	0.26	0.28	0.14	0.90	0.89	0.44	0.25	0.78	0.92	0.41	
FU-DR01-03	Utu Uli	MC*	52.89	0.03	0.06	–	0.47	3.93	0.31	2.13	–	–	–	–
FU-DR01-03	Utu Uli	MC*	52.88	0.10	0.07	–	0.54	3.45	0.33	2.64	–	–	–	–
FU-DR01-03	Utu Uli	MC	53.78	0.10	0.07	–	1.78	1.91	0.79	1.65	1.04	–	1.23	–
FU-DR01-03	Utu Uli	MC	49.87	0.59	0.27	0.18	0.67	3.73	0.24	1.56	–	–	4.95	–
FU-PL08-06	Utu Uli	MC	48.03	0.13	0.19	0.57	2.10	2.27	0.58	2.21	0.80	3.31	0.37	–
FU-PL08-05	Utu Uli	MC	52.36	0.34	0.06	–	1.62	3.07	0.61	1.13	0.58	–	2.18	–
FU-PL08-03	Utu Uli	MC	51.20	0.49	0.05	–	1.29	2.80	0.83	1.05	0.12	–	3.65	–
FU-DR15-10	Anakele	MC	47.37	0.32	0.14	0.31	0.84	3.89	0.72	1.21	3.54	2.80	0.29	–
FU-DR15-10	Anakele	MC	41.81	–	0.03	0.07	0.55	3.87	0.39	0.90	0.79	2.28	0.55	–
FU-DR15-10	Anakele	MC	49.40	–	–	–	0.51	3.41	1.06	0.97	2.11	0.76	0.17	–
FU-DR15-10	Anakele	MC	51.57	–	–	0.25	0.16	6.34	0.29	0.26	0.44	–	–	–
FU-DR15-10	Anakele	MC	43.80	–	–	–	0.46	2.85	0.58	1.02	1.63	0.22	0.09	–
FU-DR22-03	Utu Sega	MC	43.16	0.20	0.31	1.44	2.10	3.06	0.43	0.88	1.52	0.86	0.67	–
FU-DR22-03	Utu Sega	MC	42.73	0.09	0.30	0.72	2.07	2.34	0.21	1.38	1.21	0.95	0.17	–
FU-DR22-03	Utu Sega	MC	43.01	0.12	0.48	1.00	2.32	1.70	0.16	2.35	2.26	1.07	0.44	–
FU-DR22-03	Utu Sega	MC	46.61	–	0.17	0.98	2.26	2.88	0.22	1.10	1.45	1.10	1.16	–
FU-DR22-03	Utu Sega	MC	46.97	–	0.26	1.25	2.83	2.41	0.17	1.24	1.55	1.27	1.22	–
Mean			47.44	0.26	0.19	0.68	1.44	3.10	0.49	1.26	1.36	1.46	1.22	
Maximum			53.78	0.59	0.48	1.44	2.83	6.34	1.06	2.35	3.54	3.31	4.95	
Minimum			41.81	0.09	0.03	0.07	0.16	1.70	0.16	0.26	0.12	0.22	0.09	
SD			3.89	0.18	0.14	0.48	0.85	1.12	0.28	0.53	0.88	0.99	1.45	
FU-PL08-06	Utu Uli	AC	44.83	0.17	0.11	0.94	2.72	2.25	0.79	1.86	5.11	1.24	0.65	–
FU-PL08-06	Utu Uli	AC	42.24	0.80	2.28	2.59	2.05	2.93	0.77	2.09	1.45	1.64	0.58	–
FU-PL08-06	Utu Uli	AC	43.38	1.23	0.64	1.90	2.50	2.35	0.62	1.45	1.52	2.44	0.62	–
FU-DR15-10	Anakele	AC	46.73	–	0.15	0.20	0.47	3.19	0.48	0.69	3.97	2.09	0.91	–
FU-DR15-10	Anakele	AC	42.17	0.47	0.27	0.18	0.53	2.75	0.39	0.91	4.67	0.97	0.49	–
FU-DR15-10	Anakele	AC	48.22	0.54	0.21	0.10	0.61	3.65	0.41	0.85	3.74	2.25	0.41	–
FU-DR22-03	Utu Sega	AC	33.45	0.25	0.59	1.07	2.23	3.13	0.40	1.69	4.00	0.63	1.01	0.22
FU-DR22-03	Utu Sega	AC	34.78	0.38	0.32	1.42	3.00	2.88	0.19	4.52	5.37	1.06	0.97	0.58
FU-DR22-03	Utu Sega	AC	37.00	0.34	0.36	1.46	3.09	2.74	0.20	4.72	4.79	1.05	1.05	0.60
Mean			41.42	0.52	0.55	1.10	1.91	2.87	0.47	2.09	3.85	1.48	0.74	0.47
Maximum			48.22	1.23	2.28	2.59	3.09	3.65	0.79	4.72	5.37	2.44	1.05	0.60
Minimum			33.45	0.17	0.11	0.10	0.47	2.25	0.19	0.69	1.45	0.63	0.41	0.22
SD			5.22	0.35	0.67	0.85	1.08	0.43	0.22	1.51	1.44	0.64	0.24	0.22

Titanium was systematically below the detection limit; '–' below detection limit; C: crystallites; MC: microcrystallites; AC: amorphous cryptocrystalline oxides; MC*: analyses of microcrystallites from the layered and massive crust.

2001). Enrichment of molybdenum in deep-sea Mn mineralization can originates from the intense leaching of volcanic rocks (Hein et al., 2008; Kuhn et al., 2003), HT sulfides (Hein et al., 2008; Krasnov et al., 1995) and/or direct adsorption from seawater (Goto et al., 2015). The fact that neither Cu nor Zn correlates with Mo indicates that sulfides were not the predominant source of Mo in our samples. Hein et al. (2008) suggested that the molybdenum enrichment recorded in the stratabound Mn samples of the Izu-Bonin arc system reflects the HT leaching of intermediate to acidic volcanic arc rocks. In the North Fiji Basin, Kuhn et al. (2003) found that the OIBs were significantly enriched in Mo compared to N-MORB (more than two orders of magnitude) suggesting that the OIBs might represent the source of Mo in their hydrothermal precipitates. Although our results do not preclude a possible seawater contribution, we favor the leaching of volcanic rocks as an explanation for the high Mo concentrations in our samples.

5.3. Model

Regardless of a likely volcanic source for the metals in the Mn oxides at Utu Uli, Anakele and Utu Sega, there are major differences in the mean concentrations of Ni, Co and Cu in the deposits. Nickel is the dominant trace metal at Utu Uli (1.45 wt.% Ni) whereas the Anakele Mn oxides samples are clearly dominated by copper (0.56 wt.% Cu) and Utu Sega Mn oxides are systematically enriched in cobalt (0.97 wt.% Co). In addition, the mean Mo concentration is significantly higher in the Utu Uli mineralization (798 ppm; Table 4) than in the Anakele and Utu Sega mineralization (respectively 425 and 532 ppm; Table 4). Several factors could explain the chemical variations between deposits: (i) mineralogical controls; (ii) source rock composition; (iii) the permeability of the volcanic edifice, rock/fluid ratios and mixing with seawater; (iv) the depth and/or the longevity of the heat source; or (v) the temperature, pH, Eh, and salinity of the hydrothermal fluids. Massive precipitation of sulfides at depth does not appear to have contributed to the chemical signature recorded in our samples since this process would have led to the entrapment of Ni, Co, Cu and Mo in high-temperature sulfide phases. In contrast, the difference in the proportion of Mn oxides may explain the higher mean Mo concentration obtained at Utu Uli than at Anakele, and in fact, when normalized for the higher fraction of Mn oxides, the mean concentrations of molybdenum are similar in the two sites. This mineralogical control by Mn oxides, however, can
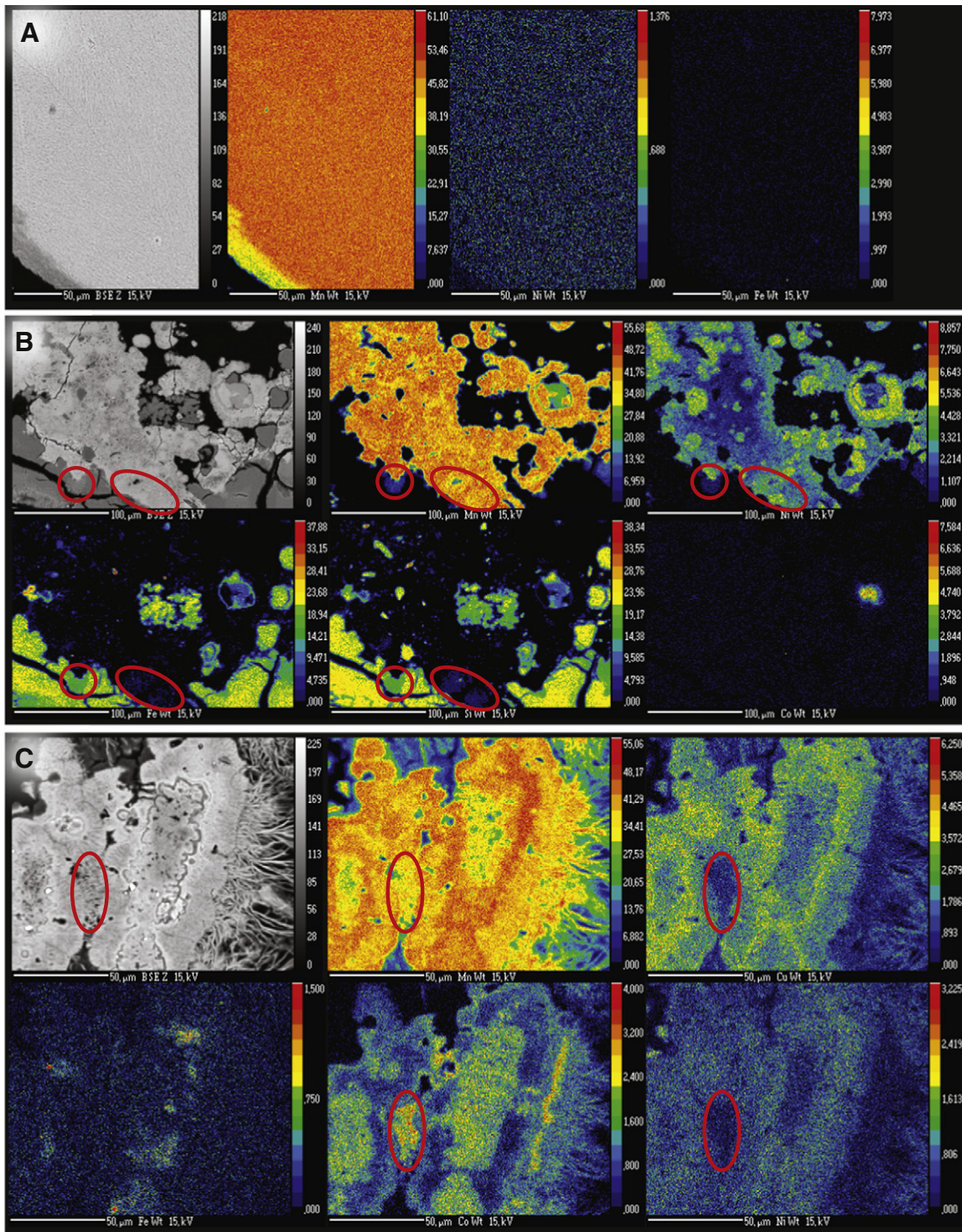
Fig. 11. Electron microprobe chemical maps of the massive layered crust (A; FU-DR01-03), Mn-cemented pyroclastic breccia (B; FU-DR01-03) and stratabound Mn oxide sample (C; FU-DR15-10). Red circles in B highlight area of nontronite replacement or the presence of residual signature of nontronite in Mn oxide. The red circle in C shows an antipathetic relationship between Co and Cu and Ni.

not explain the relatively low Mo contents in Utu Sega precipitates with respect to their high Mn concentration. N-MORBs have been identified close to Utu Sega (e.g. Alofi ridge) whereas only OIB-like basalts and E-MORB have been found near Utu Uli and Anakele (Labanieh et al., 2011). Given that OIBs can be significantly enriched in Mo compared to N-MORB (Kuhn et al., 2003), the lower molybdenum levels in the Utu Sega Mn oxides might reflect a higher proportion of an N-MORB component in the source.

Although mineralogical control and/or varying compositions of the source rocks may explain the slight chemical variations in some trace elements such as Mo, in our opinion, it cannot explain the large variations in Ni, Co and Cu in the three mineralized sites (Table 4). The structure and mineralogy at the millimeter scale reflect different pulses of hydrothermal fluids, whereas variations at the micrometric to submillimetric scales are better explained by waxing and waning of a single hydrothermal pulse (Hein et al., 2008). Given the chemical variations between the

Table 4

Comparison of mean bulk composition of Utu Uli, Anakele and Utu Sega deposits with Fe-Mn deposits from the Pacific.

	Hydrothermal								Galicia Bank* (n = 4)	Hydrogenetic Fe-Mn crusts				Pacific Fe-Mn nodules	
	Utu Uli (n = 20)	Anakele (n = 10)	Dorsale Alofi (n = 5)	Valu Fa Ridge (n = 8)	Mariana Arc (n = 26)	Tonga Arc (n = 4)	Yap Arc (n = 7)	Hawaii rift zone (n = 11)		West Pacific (n = 32)	West-central Pacific (n = 73)	East-central Pacific (n = 97)	East Pacific (n = 56)	C-C Zone (n>> 100)	Other Abyssal Plain (n>> 100)
	This study			Hein et al. (1997)					González et al. (2016)	Hein et al. (1997)				Hein et al. (1997)	
Fe/Mn	0.57	1.24	0.01	0.03	0.04	0.07	0.05	0.04		1.01	0.64	0.71	1.14	0.27	0.69
%															
Si	7.00	10.07	2.00	5.10	2.30	5.10	3.20	2.20	1.45	5.80	3.00	4.60	11.40	7.60	8.80
Al	0.78	0.57	0.96	0.24	0.72	2.50	1.10	1.00	1.03	1.40	0.71	0.88	0.88	2.90	3.00
Fe	14.62	20.40	0.60	1.30	1.70	2.70	2.20	1.90	3.08	21.80	17.00	19.20	19.20	6.90	12.70
Mn	25.52	16.50	45.22	51.60	47.20	40.40	44.20	46.40	35.90	21.60	26.60	26.90	16.90	25.40	18.50
Ca	1.47	1.13	3.95	1.70	1.80	2.30	1.50	2.00	8.74	2.90	6.40	3.40	1.90	1.70	1.80
Mg	1.42	1.31	1.86	0.57	1.90	1.80	2.40	2.70	1.72	1.20	1.20	1.20	1.20	1.70	1.40
K	0.73	0.69	0.50	0.50	1.10	0.65	1.00	1.10	0.72	0.58	0.54	0.61	0.88	1.00	0.93
Na	2.81	2.35	3.21	4.30	2.70	3.40	1.90	2.80	0.77	1.90	1.90	1.90	2.00	2.80	2.10
Ti	0.10	0.05	0.09	0.03	0.51	0.15	0.09	0.23	0.11	1.10	1.10	1.30	0.60	0.53	0.78
P	0.38	0.40	0.03	0.02	0.07	0.05	0.07	0.04	1.26	0.51	1.80	0.66	0.42	0.10	0.10
ppm															
V	288	351	414	5	203	197	529	162	2073	736	725	713	626	470	480
Co	3478	2757	9675	40	96	30	450	326	10,749	4427	7993	8110	3118	2400	2400
Ni	14,594	3590	3050	44	330	67	4518	1585	3501	3851	5728	4926	3258	12,800	6300
Cu	642	5254	4323	112	263	72	2632	83	1744	1014	1053	1187	756	10,200	4200
Zn	209	274	185	95	2574	104	1621	390	429	757	870	773	694	1400	900
As	121	129	10	16	69	20	49	21	104	286	247	290	278	159	159
Sr	352	301	356	452	561	332	851	520	2161	1703	1853	1798	1397	450	700
Y	23	25	14	12	17	23	37	14	76	207	268	228	176	133	133
Ba	478	586	320	1243	1511	507	3089	883	29,544	1695	2074	2033	4159	2800	2000
Mo	798	425	532	1658	663	394	324	312	184	445	562	532	382	520	360
Pb**	26	28	8	53	70	58	88	30	2484	1484	1809	1875	1373	450	820
Cd	10	13	16	0.8	20	6.1	44	28		2.7	4.1	3.5	3.2	12	11
Co + Ni + Cu (%)	1.87	1.16	1.70	0.02	0.07	0.02	0.76	0.20	1.60	0.93	1.48	1.42	0.71	2.54	1.29

Galicia Bank*: one stratabound crust (DRR41-1B) and three Co-rich hydrothermal Mn nodules (DRR81-1, DRR21-1 and DRR21-2).
Pb**:n = 14 (Utu Uli), n = 7 (Anakele) and n = 1 (Utu Sega).

deposits as well as within a single mineralized site or an individual sample, the hydrothermal phases and hydrothermal pulses within a single phase most likely had different temperatures, Eh, pH and salinity. The high cobalt concentrations in the Mn oxides of the Mariana and Izu-Bonin arcs are regarded as evidence for a relatively high-temperature fluid (Hein et al., 2008). Mn oxides samples at Utu Sega contain a significant amount of 10 Å manganates that are still present five years after sampling. More stable 10 Å manganates are assumed to precipitate under high-temperature conditions (Usui et al., 1989). Moreover, the chondrite-normalized REE patterns are characterized by a positive Eu anomaly which suggests (i) that the end-member fluid experienced temperature above 250 °C (e.g. Craddock et al., 2010; Douville et al., 1999; Michard, 1989; Michard and Albarède, 1986) and (ii) that mixing with seawater was restricted during the precipitation of the Mn oxides (compared to the Mn oxides at Anakele and Utu Uli). Overall, this suggests that Utu Sega Mn oxides formed at a higher temperature than the Utu Uli and Anekele Mn oxides.

In a hydrothermal system, decreasing temperature and/or chloride concentrations can results in a decrease of the concentration of Co in the hydrothermal fluids (Liu et al., 2011). This is a consequence of the destabilization of tetrahedral complexes to octahedral species that favors the precipitation of cobalt as cattierite (CoS_2) (Liu et al., 2011). In the present study, neither the SEM observations nor the electron microprobe data support the presence of cattierite in Mn oxides with high levels of cobalt. An alternative hypothesis would be that cobalt species are adsorbed more readily onto Mn oxides than nickel or copper. The preferential sorption of cobalt over nickel on manganese oxides has been demonstrated by Kay et al. (2001) in both abiotic and biotic experiments. According to this study, the first Mn oxides to form (i.e. at the highest possible temperature and/or lowest possible Eh and/or pH) would be Co-rich and characterized by a high Co/Ni ratio. At Utu Uli and Anakele, several samples display high cobalt contents (up to 2.24 wt.%). Electron microprobe chemical maps show a clear fractionation between cobalt and nickel (± copper) (Fig. 11C). The alternation between high and low cobalt concentrations observed in the Mn oxides botryoids (Fig. 11C) could reflect the waxing (high Co) and waning stages (low Co) of the hydrothermal pulses. On a broader scale, we can hypothesize that the bulk samples with high cobalt contents are indicative of a closer proximity to the major hydrothermal up-flow zones. If we assume that the chemical variations in Co, Cu and Ni observed in the botryoids (from the core to the edge; Fig. 11C) mostly reflect the physical and chemical changes in the hydrothermal fluids, then nickel can be thought to have fractionated from hydrothermal fluids at a lower temperature and/or higher Eh and/or pH (e.g. as a consequence of stronger mixing with seawater) than cobalt. Mn oxide samples characterized by very high nickel concentrations would therefore represent the distal part of high-temperature hydrothermal system. Finally, the large variations in nickel and cobalt recorded in mineralized samples from a single deposit (e.g. FU-DR01-07 and FU-DR01-08; Utu Uli; Table 1) could result from spatial and temporal variations in temperature, pH and Eh within a single mineralized site.

5.3.1. Anakele and Utu Uli

The Utu Uli and Anakele Mn deposits lie on top of volcanic edifices and are intimately associated with basaltic pyroclastic rocks. The hydrothermal character of the mineralization is evident since the Fe-Si-Mn precipitates are clearly different in terms of morphology, microstructure, crystallinity, mineralogical and geochemical composition than percipitates resulting form hydrogenetic and diagenetic mineralization. Magmatic sills and dike intrusions in the volcanoes probably produced the hydrothermal circulation. Large volumes of seawater may have circulated through extensive conduits resulting from the high porosity of the host rocks. Major textural and mineralogical changes to the host rocks have been observed in several subsurface samples. Since degradation of pyroclasts and volcanic glass is enhanced by increased

temperature, the strong and pervasive alteration of the host rocks argues for the percolation of a HT fluid (≥150 °C) during the waxing stages of some hydrothermal pulses (Hein et al., 2008). However, a direct CO_2 contribution from magmatic fluids, though hypothetical, may have promoted leaching of the volcanic rocks at a relatively low temperature (Escoube et al., 2015). Thus, hot modified seawater, generated by convective hydrothermal circulation driven by the heat of magma bodies, is inferred to have leached the basaltic rocks and provided the trace elements (including metals) to the fluids.

The local geological setting (e.g. the depth of mineralization, the relationships with pyroclastic volcanoes, and the influence of hotspot on the magmatic products) suggests that the first stage of the hydrothermal activity at Utu Uli and Anakele might have been similar to hydrothermal activity at Loihi seamount. At Loihi, the warm (up to 55 °C) vent solutions are enriched in Fe, Mn, Si, CH_4, CO_2 and possibly Ni (Sedwick et al., 1992).According to Sedwick et al. (1994, 1992) the compositions of these warm fluids are consistent with sub-seafloor mixing of a high-temperature (>200 °C) hydrothermal fluids with seawater, together with the addition of magmatic volatiles (CO_2 and SO_2) (Wheat et al., 2000). High CO_2 leads to low pH (pH < 5.5) and high alkalinity, which promotes alteration of the volcanic rocks (Escoube et al., 2015; Sedwick et al., 1992).The green and yellow-orange to reddish deposits formed at or near the seafloor as the hydrothermal fluids mixed with seawater (De Carlo et al., 1983). Nontronite, Fe-montmorillonite, lepidocrocite and X-ray amorphous Fe oxides and silica are the main mineral phases identified (De Carlo et al., 1983). If we assume that a similar process occurred at Utu Uli and Anakele, then Fe-rich smectite, iron oxyhydroxides and opal would have been the first mineral phases to precipitate. If the LT fluids were similar to those of Loihi, they would have been enriched in Fe, Mn, Si and Ni relative to seawater and hydrothermal fluids from the mid-ocean ridge (Sedwick et al., 1992). A decrease in hydrothermal activitycould have driven the oxidation of Mn(II) on the seafloor, leading to the development of the layered manganese crust. This crust has low to very low trace metals contents and was probably formed by precipitation of manganese oxides in an open system, where significant quantities of metals would have been lost in the water column. This widespread and ~2-cm-thick Mn layer might have sealed the hydrothermal system and trapped the metals-rich hydrothermal fluids (e.g. Fouquet et al., 1993), promoting their adsorption on Mn oxides. Successive hydrothermal pulses and related waning and waxing stages might have produced the textural (i.e. intercalation of AC, MC and C oxides) and geochemical (decoupling of Co, Cu and Ni) diversity of the cement-like Mn oxides; the Co-rich AC and MC oxides reflecting the higher-temperature hydrothermal pulses and Ni-rich MC and C Mn oxides reflecting the lower-temperature hydrothermal pulses. The Mn oxides progressively infilled the pore spaces and replaced the Fe-rich smectite, eventually forming a near pure Mn mineralization, up to 10-cm-thick and strongly enriched in Ni and/or Cu and/or Co. Subsequent high-temperature hydrothermal stages led to fracturing of the layered Mn crust and the precipitation of Fe-Si-rich crests and/or veins at the seafloor.

These processes operating at the subsurface level are still largely unknown. However, the high Ni, Co and Cu contents in the Mn oxides suggest that the precipitation of massive HT sulfides bodies at depth was limited. The low barium and strontium concentrations compared to other hydrothermal Mn oxides deposits (Table 4) might reflect the precipitation of barite at depth. At Loihi, barite-rich sulfate mineralization with sulfides were sampled after the collapse of the summit crater in 1996 (Davis et al., 2003; Davis and Clague, 1998). The bulk composition of these hydrothermal samples shows high concentrations of Ba, Sr, Zn and Pb (Davis et al., 2003), elements which are systematically depleted in the Mn oxides at Utu Uli and Anakele. Even though further studies are required, the precipitation of minor barite and zinc sulfide or sulfates at depth might explain the absence of major Ba, Sr, and Zn enrichment in the Mn oxides at Utu Uli and Anakele.

5.3.2. Utu Sega

Little is known about the local geology and the morphology of the mineralization at Utu Sega. From the dredge haul, we might infer that the host rocks are mainly composed of strongly altered volcanic breccias and lavas and sediments. The structure, mineralogy and texture of the Mn oxide sample resemble the stratabound Mn oxides described by Hein et al. (2008, 1996, 1990) in arc and intraplate settings. However, the chemical data of the Utu Sega Mn oxide differ significantly from the data reported for the stratabound Mn deposits. Cobalt is highly enriched at Utu Sega and REE chondrite-normalized patterns display a positive Eu anomaly, which is considered to be diagnostic of a high-temperature influence (e.g. Craddock et al., 2010; Douville et al., 1999; Michard, 1989; Michard and Albarède, 1986). Coupled with the high stability of 10 Å manganates after five years which is characteristic of HT Mn mineralization (Usui et al., 1989), this evidence points to precipitation close to the hydrothermal source. More focused hydrothermal activity, similar to that seen at the Lau basin deposits (i.e. Hine Hina and Vai Lili; Fouquet et al., 1993), might therefore be proposed. However, in the Lau basin, the subsurface precipitation of high-temperature sulfides has prevented any Co, Ni and Cu enrichment in the Mn oxide crusts, which is obviously not the case at Utu Sega. Finally, the Mn oxides samples studied here share common features with the stratabound Mn layers and Mn nodules of the Galicia Bank (González et al., 2016). The latter, which exhibit high Co concentrations and strong positive europium anomalies (Table 4) are thought to have been derived from ascending metal-rich hydrothermal fluids that leached the basement rocks and/or organic-matter-rich sediments (González et al., 2016). A potential on-shore analog for the Utu Sega deposit can be found in the Calatrava Volcanic Field (CVF; Spain) (Crespo et al., 1995; Crespo and Lunar, 1997). The CVF Mn-rich samples have high cobalt concentrations (up to 1.7 wt.%) and sometimes high Cu (up to 0.87 wt.%) and high Ni (up to 0.62 wt.%) concentrations. The highest Co concentrations are recorded in samples with high Fe; however the iron oxides mineralization occurred after deposition of Co-rich Mn oxides (Crespo et al., 1995). Crespo et al. (1995) and Crespo and Lunar (1997) proposed a volcanogenic-hydrothermal origin for the CVF mineralization. Metals were thought to have been transported by epithermal hydrothermal solutions with high fO_2 and scavenged by Mn oxides in close proximity to the volcanic emission centers and normal faults.

Additional detailed studies (e.g. submersible dives) at Utu Sega are required to constrain the genetic model for this atypical type of mineralization.

5.4. Resources considerations

The mean nickel, copper and cobalt contents (Table 4) are 1 to 2 orders of magnitude greater than most hydrothermal manganese mineralization so far studied in the deep sea. Furthermore, the mean concentrations of base metals are similar to if not greater than those reported for hydrogenetic crusts (Table 4). The Utu Uli deposit displays the most striking enrichments, especially in terms of the mean nickel concentration (>1.45 wt.%), which exceeds the mean nickel contents of nodules found in the Clarion-Clipperton fracture zone.

Hydrothermal manganese deposits are commonly considered to be less economically important and valuable only as an indicator for polymetallic sulfide exploration (Usui and Someya, 1997). Given the estimated mineralized area (~1.5 km^2), a mean thickness of ~5 cm and the mean concentration of Mn, Ni, Co and Cu, Utu Uli and Anakele might hold up to 38,200 t and 27,000 t of Mn, 2200 t and 580 t of Ni, 520 t and 450 t of Co, 100 t and 840 t of Cu, respectively.

Even though these calculations are only rough estimates and should be treated with caution given the high uncertainties, they nevertheless demonstrate that, in specific contexts, oceanic hydrothermal Mn-Fe-Si deposits may host significant amounts of metals. New exploration campaigns are now required to locate other deposits and to evaluate if this type of low-tonnage Mn deposits could provide a potential long-term resource.

5.5. Implications on the trace metal budgets of the ocean

Hydrothermal venting has long been known to provide significant fluxes of chemicals to the ocean (e.g. Edmond et al., 1979) even if its impact on the chemical composition of seawater is still poorly constrained (Sander and Koschinsky, 2016). LT venting accounts for a significant portion of heat flux along a mid-ocean ridge but is considered to be a simple mixtures of bottom seawater and a high-temperature end member (Wheat et al., 2000), with a relatively homogeneous composition and very low metal concentrations. Studies of diffuse venting at Loihi illustrate that low temperature hydrothermal fluids can have a wide range of compositions and possible impacts on the fluxes of some elements (e.g. CO_2, Mg, sulfates and K; Wheat et al., 2000). In this study, we identified LT Mn-Fe-Si mineralization that precipitates from a Ni-, Co-, Cu-rich LT hydrothermal fluid. A loss of metals in the water column is expected in the first stages of the hydrothermal activity, prior to isolation of the system (see Section 5.3.1). A recent study (Atkins et al., 2014) has shown that aging of metal-rich birnessite might provide trace metals (e.g. nickel) to the seawater. In this way, a late release of metals to seawater might also occur long after the cessation of hydrothermal activity. This type of metal-rich hydrothermal fluid and precipitates is not restricted to our study area since hydrothermal Mn mineralization with minor to major metal enrichments have also been described in continental margin (González et al., 2016), hotspot (Hein et al., 1996; Moore and Vogt, 1976), arc (Hein et al., 2008, 1992) and back-arc (Kuhn et al., 2003) settings. Since LT hydrothermal activity is difficult to detect using conventional sensors, this kind of processes could well be widespread in deep-sea environments. Even though the impact on oceanic trace metals cycles is uncertain, the impact of metal-rich low temperature hydrothermal fluids and precipitates should be considered in future studies of the biogeochemical cycle of metals in the ocean.

6. Conclusions

The Utu Uli, Anakele and Utu Sega deposits discovered during the FUTUNA cruise (2010) are unusual in that they contain high concentrations of transition metals (i.e., Ni, Co, Cu). These deposits outcrop on top of volcanoes and formed in close association with the volcanic facies. In-situ observations and mineralogical and geochemical studies clearly support a hydrothermal origin for the mineralization. The manganese mineralization occurs as massive layered crust and Mn-cement in strongly altered pyroclastic rocks, brecciated lavas and, in rare cases, in sandstones. Relatively large hydrothermal cells (up to a few hundreds of meters) developed within the highly porous volcanic edifices, driven by the heat from the magmatic dikes and sills. The wide distribution of the Mn mineralization is most likely related to the high permeability of the host rocks and strong mixing of the hydrothermal fluids with seawater. Nickel, cobalt and copper enrichments are clearly controlled by the precipitation of 7 Å and 10 Å manganates. Several parameters might explain the enrichment of metals in our hydrothermal ferromanganese deposits: (i) a lack of precipitation of HT massive sulfides at depths that would have retained Ni, Co and Cu (Glasby et al., 1997); (ii) entrapment of metals at subsurface levels, preventing metal losses in the water column (Fouquet et al., 1993); and (iii) the ability of birnessite and buserite/todorokite to scavenge Co, Ni, and Cu from solutions (Post, 1999). Metal loss in the water column during the early stages of the hydrothermal activity can account for the depleted character of the dense layered Mn crust that precipitates on the seafloor. We assume that this layer, which covers large areas at the surface, formed a cap at the seawater/seafloor interface that eventually trapped the hydrothermal fluid (Fouquet et al., 1993). The isolation of the hydrothermal system led to the retention of Ni, Cu, and Co at subsurface levels

promoting their adsorption onto the manganese oxyhydroxides. The large chemical variations in trace metals in Mn oxides among and within deposits most likely reflect changes in physical and chemical conditions (e.g. T°, pH, Eh, salinity) in the hydrothermal fluids over space and time. The Utu Uli and Anakele mineralization might be the result of an evolution in hydrothermal activity similar to that presently occurring at Loihi seamount. Elsewhere, the Co-rich Mn deposits of the Calatrava Volcanic Field (CVF; Spain) and the Co-rich nodules of the Galicia Bank (González et al., 2016) are perhaps the most likely analogs of mineralization at Utu Sega. The CVF Mn-(Co) deposits formed in close proximity to Pliocene volcanic rocks. Metals were transported by epithermal hydrothermal solutions with high fO_2 and cobalt was scavenged by Mn oxides (Crespo et al., 1995; Crespo and Lunar, 1997).

A recent study (Atkins et al., 2014) has shown that aging of metal-rich birnessite might provide a source of trace metals (e.g. nickel) to seawater. Consequently, metal-rich LT diffuse flow vents might represent a significant source of metals in seawater via direct losses in the water column and/or indirect release during aging of enriched manganates. Given that Mn mineralization and LT hydrothermal fluids (Sakai et al., 1987) with minor to major metal enrichments are known to occur in a variety ofsettings (González et al., 2016; Hein et al., 2008, 1996, 1992; Kuhn et al., 2003; Moore and Vogt, 1976), and the fact that LT hydrothermal activity is difficult to detect using conventional sensors, we suggest that this kind of processes could be widespread in deep-sea environments. If so, the metal-rich LT hydrothermal activity may be of major importance for future research on the net flux of hydrothermally derived trace metals (e.g. Ni, Co, Cu) to the open ocean.

Supplementary data to this article can be found online at http://dx.doi.org/10.1016/j.oregeorev.2016.09.014.

Author contributions

Y.F. conceived the project and participated as chief scientist in the FUTUNA cruise (R/V L'Atalante). J.E., S.C. performed sample/chemical preparation and analyzed the samples (XRD, ED-XRF and WD-XRF). J.L. and E.P. analyzed the manganates (electron microprobe). E.P. wrote the article. All authors contributed to discussions, interpretation of the results and writing of the manuscript.

Competing financial interests

The authors declare no competing financial interests.

Acknowledgments

References

Alibo, D.S., Nozaki, Y., 1999. Rare earth elements in seawater: particle association, shale-normalization, and Ce oxidation. Geochim. Cosmochim. Acta 63, 363–372. http://dx.doi.org/10.1016/S0016-7037(98)00279-8.

Atkins, A.L., Shaw, S., Peacock, C.L., 2014. Nucleation and growth of todorokite from birnessite: implications for trace-metal cycling in marine sediments. Geochim. Cosmochim. Acta 144, 109–125. http://dx.doi.org/10.1016/j.gca.2014.08.014.

Bau, M., Schmidt, K., Koschinsky, A., Hein, J., Kuhn, T., Usui, A., 2014. Discriminating between different genetic types of marine ferro-manganese crusts and nodules based on rare earth elements and yttrium. Chem. Geol. 381, 1–9. http://dx.doi.org/10.1016/j.chemgeo.2014.05.004.

Bonatti, E., Kraemer, T., Rydell, H., 1972. Classification and genesis of submarine iron-manganese deposits. In: Horn, D.R. (Ed.), Ferromanganese Deposits of the Ocean Floor. Seabed Assessment Program, IDOE, NSF, Washington D.C., USA, pp. 149–166.

Burns, R.G., Burns, V.M., 1977. Chapter 7 mineralogy. In: Glasby, G.P. (Ed.), Elsevier Oceanography Series. Marine Manganese Deposits. Elsevier, pp. 185–248.

Choi, J.H., Hariya, Y., 1992. Geochemistry and depositional environment of Mn oxide deposits in the Tokoro Belt, northeastern Hokkaido. Japan Econ. Geol. 87, 1265–1274. http://dx.doi.org/10.2113/gsecongeo.87.5.1265.

Conly, A.G., Scott, S.D., Bellon, H., 2011. Metalliferous manganese oxide mineralization associated with the Boléo Cu-Co-Zn District. Mexico Econ. Geol. 106, 1173–1196. http://dx.doi.org/10.2113/econgeo.106.7.1173.

Craddock, P.R., Bach, W., Seewald, J.S., Rouxel, O.J., Reeves, E., Tivey, M.K., 2010. Rare earth element abundances in hydrothermal fluids from the Manus Basin, Papua New Guinea: indicators of sub-seafloor hydrothermal processes in back-arc basins. Geochim. Cosmochim. Acta 74, 5494–5513. http://dx.doi.org/10.1016/j.gca.2010.07.003.

Crespo, A., Lunar, R., 1997. Terrestrial hot-spring Co-rich Mn mineralization in the Pliocene-quaternary Calatrava region (Central Spain). Geol. Soc. Lond. Spec. Publ. 119, 253–264. http://dx.doi.org/10.1144/GSL.SP.1997.119.01.16.

Crespo, A., Lunar, R., Oyarzuc, R., Doblas, M., 1995. Unusual case of hot springs-related Co-rich Mn mineralization in Central Spain; the Pliocene Calatrava deposits. Econ. Geol. 90, 433–437. http://dx.doi.org/10.2113/gsecongeo.90.2.433.

Cronan, D.S., 1997. Some controls on the geochemical variability of manganese nodules with particular reference to the tropical South Pacific. Geol. Soc. Lond. Spec. Publ. 119, 139–151. http://dx.doi.org/10.1144/GSL.SP.1997.119.01.10.

Davis, A.S., Clague, D.A., 1998. Changes in the hydrothermal system at Loihi seamount after the formation of Pele's pit in 1996. Geology 26, 399–402. http://dx.doi.org/10.1130/0091-7613(1998)026<0399:CITHSA>2.3.CO;2.

Davis, A.S., Clague, D.A., Zierenberg, R.A., Wheat, C.G., Cousens, B.L., 2003. Sulfide formation related to changes in the hydrothermal system on Loihi seamount, Hawai'i, following the seismic event in 1996. Can. Mineral. 41, 457–472. http://dx.doi.org/10.2113/gscanmin.41.2.457.

De Carlo, E.H., McMurtry, G.M., Yeh, H.-W., 1983. Geochemistry of hydrothermal deposits from Loihi submarine volcano. Hawaii Earth Planet. Sci. Lett. 66, 438–449. http://dx.doi.org/10.1016/0012-821X(83)90157-7.

Douville, E., Bienvenu, P., Charlou, J.L., Donval, J.P., Fouquet, Y., Appriou, P., Gamo, T., 1999. Yttrium and rare earth elements in fluids from various deep-sea hydrothermal systems. Geochim. Cosmochim. Acta 63, 627–643. http://dx.doi.org/10.1016/S0016-7037(99)00024-1.

Douville, E., Charlou, J.L., Oelkers, E.H., Bienvenu, P., Jove Colon, C.F., Donval, J.P., Fouquet, Y., Prieur, D., Appriou, P., 2002. The rainbow vent fluids (36°14′N, MAR): the influence of ultramafic rocks and phase separation on trace metal content in mid-Atlantic ridge hydrothermal fluids. Chem. Geol. 184, 37–48. http://dx.doi.org/10.1016/S0009-2541(01)00351-5.

Dymond, J., Lyle, M., Finney, B., Piper, D.Z., Murphy, K., Conard, R., Pisias, N., 1984. Ferromanganese nodules from MANOP sites H, S, and R—control of mineralogical and chemical composition by multiple accretionary processes. Geochim. Cosmochim. Acta 48, 931–949. http://dx.doi.org/10.1016/0016-7037(84)90186-8.

Edmond, J.M., Measures, C., Mangum, B., Grant, B., Sclater, F.R., Collier, R., Hudson, A., Gordon, L.I., Corliss, J.B., 1979. On the formation of metal-rich deposits at ridge crests. Earth Planet. Sci. Lett. 46, 19–30. http://dx.doi.org/10.1016/0012-821X(79)90062-1.

Escoube, R., Rouxel, O.J., Edwards, K., Glazer, B., Donard, O.F.X., 2015. Coupled Ge/Si and Ge isotope ratios as geochemical tracers of seafloor hydrothermal systems: case studies at Loihi seamount and East Pacific rise 9°50′N. Geochim. Cosmochim. Acta 167, 93–112. http://dx.doi.org/10.1016/j.gca.2015.06.025.

Fouquet, Y., Stackelberg, U.v., Charlou, J.L., Erzinger, J., Herzig, P.M., Muehe, R., Wiedicke, M., 1993. Metallogenesis in back-arc environments; the Lau Basin example. Econ. Geol. 88, 2154–2181. http://dx.doi.org/10.2113/gsecongeo.88.8.2154.

Fouquet, Y., Cambon, P., Etoubleau, J., Charlou, J.L., OndréAs, H., Barriga, F.J.A.S., Cherkashov, G., Semkova, T., Poroshina, I., Bohn, M., Donval, J.P., Henry, K., Murphy, P., Rouxel, O., 2010. Geodiversity of hydrothermal processes along the mid-Atlantic ridge and ultramafic-hosted mineralization: a new type of oceanic Cu-Zn-Co-Au volcanogenic massive sulfide deposit. In: Rona, P.A., Devey, C.W., Dyment, J., Murton, B.J. (Eds.), Diversity of Hydrothermal Systems on Slow Spreading Ocean Ridges. American Geophysical Union, pp. 321–367.

Fouquet, Y., Alix, A.-S., Birot, D., Chéron, S., Charlou, J.L., Donval, J.-P., Etoubleau, J., Germain, Y., Guillou, M., Guerin, C., Guyader, V., Konn, C., Labanieh, S., Pelleter, E., Pierre, D., Dupré, S., Scalabrin, C., Cambon, M.-A., Menot, L., Pradillon, F., Chazot, G., Dyment, J., Szitkar, F., Gouin, J., 2015. Discovery of extensive hydrothermal fields in the Wallis and Futuna back-arc environment (SW Pacific). In: André-Mayer, A.-S., Cathelineau, M., Muchez, P., Pirard, E., Sindern, S. (Eds.), Mineral Resources in a Sustainable World, Proceedings of the 13th Biennial SGA Meeting, 24–27 August 2015, pp. 1223–1226.

Glasby, G.P., Stüben, D., Jeschke, G., Stoffers, P., Garbe-Schönberg, C.D., 1997. A model for the formation of hydrothermal manganese crusts from the Pitcairn Island hotspot. Geochim. Cosmochim. Acta 61, 4583–4597. http://dx.doi.org/10.1016/s0016-7037(97)00262-7.

González, F.J., Somoza, L., Hein, J.R., Medialdea, T., León, R., Urgorri, V., Reyes, J., Martín-Rubí, J.A., 2016. Phosphorites, Co-rich Mn nodules, and Fe-Mn crusts from Galicia Bank, NE Atlantic: reflections of Cenozoic tectonics and paleoceanography. Geochem. Geophys. Geosyst. 17, 346–374. http://dx.doi.org/10.1002/2015GC005861.

Goto, K.T., Shimoda, G., Anbar, A.D., Gordon, G.W., Harigane, Y., Senda, R., Suzuki, K., 2015. Molybdenum isotopes in hydrothermal manganese crust from the Ryukyu arc system: implications for the source of molybdenum. Mar. Geol. 369, 91–99. http://dx.doi.org/10.1016/j.margeo.2015.08.007.

Hein, J.R., Schulz, M.S., Kang, J.-K., 1990. Insular and submarine ferromanganese mineralization of the Tonga-Lau region. Mar. Min. 9, 305–354.

Hein, J.R., Ahn, J.-H., Wong, J.C., Kang, J.-K., Smith, V.K., Yoon, S.-H., d'Angelo, W.M., Yoo, S.-O., Gibbs, A.E., Kim, H.-J., Quinterno, P.J., Jung, M.-Y., Davis, A.S., Park, B.-K., Gillison, J.R., Marlow, M.S., Schulz, M.S., Siems, D.F., Taggart, J.E., Rait, N., Pickthorn, L.G., Malcolm, M.J., Kavulak, M.G., Yeh, H.-W., Mann, D.M., Noble, M.A., Riddle, G.O., Roushey, B.H., Smith, H., 1992. Geology, Geophysics, Geochemistry, and Deep-sea Mineral Deposits, Federated States of Micronesia KORDI-USGS R.V. Farnella Cruise F11-90-CP (USGS Numbered Series No. 92–218), Open-File Report U.S. Geological Survey.

Hein, J.R., Gibbs, A.E., Clague, D.A., Torresan, M., 1996. Hydrothermal mineralization along submarine rift zones. Hawaii Mar. Georesour. Geotechnol. 14, 177–203.

Hein, J.R., Koschinsky, A., Halbach, P., Manheim, F.T., Bau, M., Kang, J.-K., Lubick, N., 1997. Iron and manganese oxide mineralization in the Pacific. Geol. Soc. Lond. Spec. Publ. 119, 123–138. http://dx.doi.org/10.1144/GSL.SP.1997.119.01.09.

Hein, J.R., Koschinsky, A., Bau, M., Manheim, F.T., Kang, J.-K., Roberts, L., 2000. Cobalt-rich ferromanganese crusts in the Pacific. Handbook of Marine Mineral Deposits. CRC Press, pp. 239–279.

Hein, J.R., Schulz, M.S., Dunham, R.E., Stern, R.J., Bloomer, S.H., 2008. Diffuse flow hydrothermal manganese mineralization along the active Mariana and southern Izu-Bonin arc system, western Pacific. J. Geophys. Res. 113, B08S14. http://dx.doi.org/10.1029/2007jb005432.

Hein, J.R., Mizell, K., Koschinsky, A., Conrad, T.A., 2013. Deep-ocean mineral deposits as a source of critical metals for high- and green-technology applications: comparison with land-based resources. Ore Geol. Rev. 51, 1–14. http://dx.doi.org/10.1016/j.oregeorev.2012.12.001.

Hein, J.R., Spinardi, F., Okamoto, N., Mizell, K., Thorburn, D., Tawake, A., 2015. Critical metals in manganese nodules from the Cook Islands EEZ, abundances and distributions. Ore Geol. Rev. 68, 97–116. http://dx.doi.org/10.1016/j.oregeorev.2014.12.011.

Josso, P., Pelleter, E., Pourret, O., Fouquet, Y., Cherone, S., Bollinger, C., 2016. A new discrimination scheme for oceanic Ferromanganese deposits using high field strength and rare earth elements. Ore Geol. Rev. 87, 3–15.

Kay, J.T., Conklin, M.H., Fuller, C.C., O'Day, P.A., 2001. Processes of nickel and cobalt uptake by a manganese oxide forming sediment in Pinal Creek, Globe Mining District, Arizona. Environ. Sci. Technol. 35, 4719–4725. http://dx.doi.org/10.1021/es010514d.

Krasnov, S.G., Cherkashev, G.A., Stepanova, T.V., Batuyev, B.N., Krotov, A.G., Malin, B.V., Maslov, M.N., Markov, V.F., Poroshina, I.M., Samovarov, M.S., Ashadze, A.M., Lazareva, L.I., Ermolayev, I.K., 1995. Detailed geological studies of hydrothermal fields in the North Atlantic. Geol. Soc. Lond. Spec. Publ. 87, 43–64. http://dx.doi.org/10.1144/GSL.SP.1995.087.01.05.

Krauskopf, K.B., 1957. Separation of manganese from iron in sedimentary processes. Geochim. Cosmochim. Acta 12, 61–84. http://dx.doi.org/10.1016/0016-7037(57)90018-2.

Kuhn, T., Bau, M., Blum, N., Halbach, P., 1998. Origin of negative Ce anomalies in mixed hydrothermal–hydrogenetic Fe–Mn crusts from the Central Indian ridge. Earth Planet. Sci. Lett. 163, 207–220. http://dx.doi.org/10.1016/S0012-821X(98)00188-5.

Kuhn, T., Bostick, B.C., Koschinsky, A., Halbach, P., Fendorf, S., 2003. Enrichment of Mo in hydrothermal Mn precipitates: possible Mo sources, formation process and phase associations. Chem. Geol. 199, 29–43. http://dx.doi.org/10.1016/S0009-2541(03)00054-8.

Labanieh, S., Chazot, G., Etoubleau, J., Fouquet, Y., Dosso, L., Hemond, C., 2011. Origin of the seamounts near Futuna Island, SW Pacific. Mineral. Mag. 75, 1261.

Liu, W., Borg, S.J., Testemale, D., Etschmann, B., Hazemann, J.-L., Brugger, J., 2011. Speciation and thermodynamic properties for cobalt chloride complexes in hydrothermal fluids at 35–440 °C and 600 bar: an in-situ XAS study. Geochim. Cosmochim. Acta 75, 1227–1248. http://dx.doi.org/10.1016/j.gca.2010.12.002.

Manheim, F.T., Lanebostwick, C.M., 1988. Cobaltinferromanganesecrustsas a monitorofhydrothermaldischargeon thepacific sea-floor. Nature 335, 59–62.

Michard, A., 1989. Rare earth element systematics in hydrothermal fluids. Geochim. Cosmochim. Acta 53, 745–750. http://dx.doi.org/10.1016/0016-7037(89)90017-3.

Michard, A., Albarède, F., 1986. The REE content of some hydrothermal fluids. Chem. Geol. 55, 51–60. http://dx.doi.org/10.1016/0009-2541(86)90127-0.

Moorby, S.A., Cronan, D.S., Glasby, G.P., 1984. Geochemistry of hydrothermal Mn-oxide deposits from the S.W. Pacific island arc. Geochim. Cosmochim. Acta 48, 433–441. http://dx.doi.org/10.1016/0016-7037(84)90272-2.

Moore, W.S., Vogt, P.R., 1976. Hydrothermal manganese crusts from two sites near the Galapagos spreading axis. Earth Planet. Sci. Lett. 29, 349–356. http://dx.doi.org/10.1016/0012-821X(76)90139-4.

Nicholson, K., 1992. Contrasting mineralogical-geochemical signatures of manganese oxides; guides to metallogenesis. Econ. Geol. 87, 1253–1264. http://dx.doi.org/10.2113/gsecongeo.87.5.1253.

Pelletier, B., Lagabrielle, Y., Benoit, M., Cabioch, G., Calmant, S., Garel, E., Guivel, C., 2001. Newly identified segments of the Pacific–Australia plate boundary along the North Fiji transform zone. Earth Planet. Sci. Lett. 193, 347–358. http://dx.doi.org/10.1016/S0012-821X(01)00522-2.

Post, J.E., 1999. Manganese oxide minerals: crystal structures and economic and environmental significance. Proc. Natl. Acad. Sci. 96, 3447–3454. http://dx.doi.org/10.1073/pnas.96.7.3447.

Pouchou, J.L., Pichoir, F., 1988. A simplified version of the "PAP" model for matrix corrections in EPMA. Microbeam Anal. 315, 138.

Rogers, T.D.S., Hodkinson, R.A., Cronan, D.S., 2001. Hydrothermal manganese deposits from the Tonga-Kermadec ridge and Lau Basin region, Southwest Pacific. Mar. Georesour. Geotechnol. 19, 245–268. http://dx.doi.org/10.1080/106411901753335326.

Sakai, H., Tsubota, H., Nakai, T., Ishibashi, J., Akagi, T., Gamo, T., Tilbrook, B., Igarashi, G., Kodera, M., Shitashima, K., Nakamura, S., Fujioka, K., Watanabe, M., McMurty, G., Malahoff, A., Ozima, M., 1987. Hydrothermal activity on the summit of Loihi seamount. Hawaii Geochem. J. 21, 11–21. http://dx.doi.org/10.2343/geochemj.21.11.

Sander, S.G., Koschinsky, A., 2016. The export of iron and other trace metals from hydrothermal vents and the impact on their marine biogeochemical cycle. In: Demina, L.L., Galkin, S.V. (Eds.), Trace Metal Biogeochemistry and Ecology of Deep-sea Hydrothermal Vent SystemsThe Handbook of Environmental Chemistry. Springer International Publishing, pp. 9–24.

Sedwick, P.N., McMurtry, G.M., Macdougall, J.D., 1992. Chemistry of hydrothermal solutions from Pele's vents, Loihi seamount. Hawaii Geochim. Cosmochim. Acta 56, 3643–3667. http://dx.doi.org/10.1016/0016-7037(92)90159-G.

Sedwick, P.N., McMurtry, G.M., Hilton, D.R., Goff, F., 1994. Carbon dioxide and helium in hydrothermal fluids from Loihi seamount, Hawaii, USA: Temporal variability and implications for the release of mantle volatiles. Geochim. Cosmochim. Acta 58, 1219–1227. http://dx.doi.org/10.1016/0016-7037(94)90587-8.

Sun, S., McDonough, W.F., 1989. Chemical and isotopic systematics of oceanic basalts: implications for mantle composition and processes. Geol. Soc. Lond. Spec. Publ. 42, 313–345. http://dx.doi.org/10.1144/GSL.SP.1989.042.01.19.

Toth, J.R., 1980. Deposition of submarine crusts rich in manganese and iron. Geol. Soc. Am. Bull. 91, 44–54. http://dx.doi.org/10.1130/0016-7606(1980)91<44:DOSCRI>2.0.CO;2.

Usui, A., Someya, M., 1997. Distribution and composition of marine hydrogenetic and hydrothermal manganese deposits in the northwest Pacific. Geol. Soc. Lond. Spec. Publ. 119, 177–198. http://dx.doi.org/10.1144/GSL.SP.1997.119.01.12.

Usui, A., Mellin, T.A., Nohara, M., Yuasa, M., 1989. Structural stability of marine 10 Å manganates from the Ogasawara (Bonin) arc: implication for low-temperature hydrothermal activity. Mar. Geol. 86, 41–56. http://dx.doi.org/10.1016/0025-3227(89)90017-0.

Wheat, C.G., Jannasch, H.W., Plant, J.N., Moyer, C.L., Sansone, F.J., McMurtry, G.M., 2000. Continuous sampling of hydrothermal fluids from Loihi seamount after the 1996 event. J. Geophys. Res. Solid Earth 105, 19353–19367. http://dx.doi.org/10.1029/2000JB900088.